
15 **An improved regional coupled modeling system for Arctic sea ice simulation and**
16 **prediction: a case study for 2018**

17

18 **Chao-Yuan Yang¹, Jiping Liu², Dake Chen¹**

19

20 ¹School of Atmospheric Sciences, Sun Yat-sen University, and Southern Marine Science and
21 Engineering Guangdong Laboratory (Zhuhai), Zhuhai, Guangdong, China

22 ²Department of Atmospheric and Environmental Sciences, University at Albany, State
23 University of New York, Albany, NY, USA

24

25 Corresponding authors:

26 Chao-Yuan Yang (yangchy36@mail.sysu.edu.cn) and Jiping Liu (jliu26@albany.edu)

27

28

删除了: a

30 **Abstract**

31 The improved/updated Coupled Arctic Prediction System (CAPS) is evaluated using a set
32 of Pan-Arctic prediction experiments for the year 2018. CAPS is built on Weather Research
33 and Forecasting model (WRF), the Regional Ocean Modeling System (ROMS), the
34 Community Ice Code (CICE), and a data assimilation based on the Local Error Subspace
35 Transform Kalman Filter. We analyze physical processes linking improved/changed physical
36 parameterizations in WRF, ROMS, and CICE to changes in the simulated Arctic sea ice state.
37 Our results show that the improved convection and boundary layer schemes in WRF result in
38 an improved simulation of downward radiative fluxes and near surface air temperature, which
39 influences the predicted ice thickness. The changed tracer advection and vertical mixing
40 schemes in ROMS reduce the bias in sea surface temperature and change ocean temperature
41 and salinity structure in the surface layer, leading to improved evolution of the predicted ice
42 extent (particularly correcting the late ice recovery issue in the previous CAPS). The improved
43 sea ice thermodynamics in CICE have noticeable influences on the predicted ice thickness. The
44 updated CAPS can better predict the evolution of Arctic sea ice during the melting season
45 compared with its predecessor, though the prediction still has some biases at the regional scale.
46 We further show that the updated CAPS can remain skillful beyond the melting season, which
47 may have potential values for stakeholders to make decisions for socioeconomical activities in
48 the Arctic.

49

50

51 1. Introduction

52 Over the past few decades, the extent of Arctic sea ice has decreased rapidly and entered
53 a thinner/younger regime associated with global climate change (e.g., Kwok, 2018; Serreze
54 and Meier, 2019). The dramatic changes in the properties of Arctic sea ice have gained
55 increasing attentions by a wide range of stakeholders, such as trans-Arctic shipping, natural
56 resource exploration, and activities of coastal communities relying on sea ice (e.g., Newton et
57 al., 2016). This leads to increasing demands on skillful Arctic sea ice prediction, particularly at
58 seasonal timescale (e.g., Jung et al., 2016; Liu et al., 2019; Stroeve et al., 2014). However,
59 Arctic sea ice predictions based on different approaches (e.g., statistical method and dynamical
60 model) submitted to the Sea Ice Outlook, a community effort managed by the Sea Ice Prediction
61 Network (SIPN, <https://www.arcus.org/sipn>), show substantial biases in the predicted seasonal
62 minimum of Arctic sea ice extent compared to the observations for most years since 2008 (Liu
63 et al., 2019; Stroeve et al., 2014).

64 Recently, we have developed an atmosphere-ocean-sea ice regional coupled modeling
65 system for seasonal Arctic sea ice prediction (Yang et al., 2020, hereafter Y20), in which the
66 Community Ice Code (CICE) is coupled with the Weather Research and Forecasting Model
67 (WRF) and the Regional Ocean Modeling System (ROMS), hereafter called Coupled Arctic
68 Prediction System (CAPS). To improve the accuracy of initial sea ice conditions, CAPS
69 employs an ensemble-based data assimilation system to assimilate satellite-based sea ice
70 observations. Seasonal Pan-Arctic sea ice predictions with improved initial sea ice conditions
71 conducted in Y20 have shown that CAPS has the potential to provide skillful Arctic sea ice

72 prediction at seasonal timescale.

73 We know that the changes of sea ice variables (e.g., ice extent, ice concentration, ice
74 thickness, ice drift) are mainly driven by forcings from the atmosphere and the ocean.
75 Atmospheric cloudiness and related radiation influence surface ice melting (Huang et al., 2019;
76 Kapsch et al., 2016; Kay et al., 2008) and the energy stored in the surface mixed layer that
77 determines the seasonal ice melt and growth (e.g., Perovich et al., 2011, 2014). Atmospheric
78 circulation is the primary driver for the transportation of sea ice and partly responsible for the
79 variability of Arctic sea ice (e.g., Mallett et al., 2021; Ogi et al., 2010; Zhang et al., 2008).
80 Olonscheck et al. (2019) suggested that atmospheric temperature fluctuations explain a
81 majority of Arctic sea ice variability while other drivers (e.g., surface winds, and poleward heat
82 transport) account for about 25% of Arctic sea ice variability. The oceanic heat inputs (as well
83 as salt inputs) into the Arctic Ocean include the Atlantic Water (AW; Aagaard, 1989;
84 McLaughlin et al., 2009) through the Barents Sea, and the Pacific Water (PW; Itoh et al., 2013;
85 Woodgate et al., 2005) from the Bering Strait. The oceanic heat inputs from AW and PW are
86 not directly available for sea ice since they are separated from a cold and fresh layer underlying
87 sea ice (e.g., Carmack et al., 2015, Fig. 2). Vertical mixing by the internal wave (e.g., Fer, 2014)
88 and double diffusion (e.g., Padman and Dillon, 1987; Turner, 1973) are the principal processes
89 for upward heat transport from the subsurface layer (i.e., AW and PW) to the surface mixed
90 layer in the Arctic Ocean. Sea ice thermodynamics determines how thermal properties of sea
91 ice (e.g., temperature, salinity) change. These changes then influence the thermal structure of
92 underlying ocean through interfacial fluxes (i.e., heat, salt and freshwater fluxes; DuVivier et

93 al., 2021; Kirkman IV and Bitz, 2011) and ice thickness (e.g., Bailey et al., 2020).

94 CAPS is configured for the Arctic with sufficient flexibility. That means each model
95 component of CAPS (WRF, ROMS, and CICE) has different physics options for us to choose
96 and capability to integrate ongoing improvements in physical parameterizations. Recently, the
97 WRF model has adapted improved convection and boundary layer schemes in the Rapid
98 Refresh (RAP) model operational at the National Centers for Environmental Prediction (NCEP,
99 Benjamin et al., 2016). The first question we want to answer in this paper is to what extent
100 these modifications can improve atmospheric simulations in the Arctic (i.e., radiation,
101 temperature, humidity, and wind), and then benefit seasonal Arctic sea ice simulation and
102 prediction. The ROMS model provides several options for tracer advection schemes. These
103 advection schemes can have different degrees of oscillatory behavior (e.g., Shchepetkin and
104 McWilliams, 1998). The oscillatory behavior can have impacts on sea ice simulation through
105 ice-ocean interactions (e.g., Naughten et al., 2017). The second question we want to answer in
106 this paper is to what extent different advection schemes can change the simulation of upper
107 ocean thermal structure and then Arctic sea ice prediction. Several recent efforts have
108 incorporated prognostic salinity into sea ice models. The CICE model has a new mushy-layer
109 thermodynamics parameterization that includes prognostic salinity and treats sea ice as a two-
110 phase mushy layer (Turner et al., 2013). Bailey et al. (2020) showed that the mushy-layer
111 physics has noticeable impacts on Arctic sea ice simulation within the Community Earth
112 System Model version 2. The third question we want to answer in this paper is whether the
113 mushy-layer scheme can produce noticeable influence on seasonal Arctic sea ice prediction.

114 Currently, SIPN focuses on Arctic sea ice predictions during the melting season, particularly
115 the seasonal minimum. It is not clear that how predictive skills of dynamical models
116 participating in SIPN may change for longer period, i.e., extending into the freezing up period,
117 which also have significance on socioeconomic aspects. The assessment of the skills of global
118 climate models (GCMs) in predicting Pan-Arctic sea ice extent with suites of hindcasts
119 suggested that GCMs may have skills at lead times of 1-6 months (e.g., Blanchard-
120 Wrigglesworth et al., 2015; Chevallier et al., 2013; Guemas et al., 2016; Merryfield et al., 2013;
121 Msadek et al., 2014; Peterson et al., 2015; Sigmond et al., 2013; Wang et al., 2013; Zampieri
122 et al., 2018). Moreover, some studies using a “perfect model” approach, which treats one
123 member of an ensemble as the truth (i.e., assuming the model is perfect without bias) and
124 analyzes the skill of other members in predicting the response of the “truth” member (e.g.,
125 Meehl et al., 2007), suggested that Arctic sea ice cover can be potentially predictable up to two
126 years in advance (e.g., Blanchard-Wrigglesworth et al., 2011; Blanchard-Wrigglesworth and
127 Bushuk, 2018; Day et al., 2016; Germe et al., 2014; Tietsche et al., 2014). The last question we
128 want to answer in this paper is whether CAPS has predictive skill for longer periods (up to 7
129 months).

130 This paper is structured as follows. Section 2 provides a brief overview of CAPS,
131 including model configurations and data assimilation procedures. Section 3 describes the
132 designs of the prediction experiments for the year of 2018 based on major improvements/
133 changes in the model components compared to its predecessor described in Y20, examines the
134 performance of the updated CAPS, and offers physical links between Arctic sea ice changes

135 and improved/changed physical parameterizations. Section 4 discusses the predictive skill of
136 CAPS at longer timescale. Discussions and concluding remarks are given in section 5.

137 **2. Coupled Arctic Prediction System (CAPS)**

138 As described in Y20, CAPS has been developed by coupling the Community Ice Code
139 (CICE) with the Weather Research and Forecasting Model (WRF) and the Regional Ocean
140 Modeling System (ROMS) based on the framework of the Coupled Ocean-Atmosphere-Wave-
141 Sediment Transport (Warner et al., 2010). The general description of each model component in
142 CAPS is referred to Y20. The advantage of CAPS is its model components have a variety of
143 physics for us to choose and capability to integrate follow-up improvements of physical
144 parameterizations. With recent achievements of community efforts, we update CAPS based on
145 newly-released WRF, ROMS, and CICE models. During this update, we focus on the Rapid
146 Refresh (RAP) physics in the WRF model, the oceanic tracer advection scheme in the ROMS
147 model, sea ice thermodynamics in the CICE model (see details in section 3), and investigate
148 physical processes linking them to Arctic sea ice simulation and prediction. The same physical
149 parameterizations described in Y20 are used here for the control simulation (see Table 1). Major
150 changes in physical parameterizations as well as the model infrastructure in the WRF, ROMS,
151 and CICE models are described in section 3.

152 As described in Y20, the Parallel Data Assimilation Framework (PDAF, Nerger and Hiller,
153 2013) was implemented in CAPS, which provides a variety of optimized ensemble-based
154 Kalman filters. The Local Error Subspace Transform Kalman Filter (LESTKF; Nerger et al.,
155 2012) is used to assimilate satellite-observed sea ice parameters. The LESTKF projects the

156 ensemble onto the error subspace and then directly computes the ensemble transformation in
157 the error subspace. This results in better assimilation performance and higher computational
158 efficiency compared to the other filters as discussed in Nerger et al. (2012).

159 The initial ensembles are generated by applying the second-order exact sampling (Pham,
160 2001) to simulated sea ice state vectors (ice concentration and thickness) from an one-month
161 free run, and then assimilating sea ice observations, including: 1) the near real-time daily Arctic
162 sea ice concentration processed by the National Aeronautics and Space Administration (NASA)
163 Team algorithm (Maslanik and Stroeve, 1999) obtained from the NSIDC
164 (<https://nsidc.org/data/NSIDC-0081/>), and 2) a combined monthly sea ice thickness derived
165 from the CryoSat-2 (Laxon et al., 2013; obtained from <http://data.seaiceportal.de>), and daily
166 sea ice thickness derived from the Soil Moisture and Ocean Salinity (SMOS; Kaleschke et al.,
167 2012; Tian-Kunze et al., 2014; obtained from [https://icdc.cen.uni-hamburg.de/en/l3c-smos-](https://icdc.cen.uni-hamburg.de/en/l3c-smos-sit.html)
168 [sit.html](https://icdc.cen.uni-hamburg.de/en/l3c-smos-sit.html)). To address the issue that sea ice thickness derived from CyroSat-2 and SMOS are
169 unavailable during the melting season, the melting season ice thickness is estimated based on
170 the seasonal cycle of the Pan-Arctic Ice Ocean Modeling and Assimilation System (PIOMAS)
171 daily sea ice thickness (Zhang and Rothrock, 2003).

172 Different from Y20, in this study, we change the localization radius from 2 to 6 grids
173 during the assimilation procedures to reduce some instability during initial Arctic sea ice
174 simulations associated with 2 localization radii. As shown in Supplementary Figure S1, the ice
175 thickness with 2 localization radii and 1.5 m uncertainty (used in Y20) shows some
176 discontinuous features (Fig. S1a), which tend to result in numerical instability during the initial

177 integration. Such discontinuous features are obviously corrected with 6 localization radii and
178 0.75 m uncertainty (Fig. S1b). Following Y20, here we test the 2018 prediction experiment
179 with 6 localization radii for the data assimilation, which shows very similar temporal evolution
180 of the total Arctic sea ice extent for the July experiment relative to that of Y20, although it (red
181 solid line) predicts slightly less ice extent than that of Y20 (blue line) (Supplementary Figure
182 S2). In this study, this configuration is designated as the reference for the following assessment
183 of the updated CAPS (hereafter Y20_MOD).

184 For the evaluation of Arctic sea ice prediction, Sea Ice Index (Fetterer et al., 2017;
185 obtained from <https://nsidc.org/data/G02135>) is used as the observed total sea ice extent, and
186 the NSIDC sea ice concentrations (SIC) derived from Special Sensor Microwave
187 Imager/Sounder (SSMIS) with the NASA Team algorithm (Cavalieri et al., 1996; obtained from
188 <https://nsidc.org/data/nsidc-0051>) is also used. For the assessment of the simulated atmospheric
189 and oceanic variables, the [European Centre for Medium-Range Weather Forecasts \(ECMWF\)](#)
190 reanalysis version 5 (ERA5; Hersbach et al., 2020; obtained from
191 <https://cds.climate.copernicus.eu>) and National Oceanic and Atmospheric Administration
192 (NOAA) Optimum Interpolation (OI) Sea Surface Temperature (SST) (Reynolds et al., 2007;
193 obtained from <https://psl.noaa.gov/data/gridded/data.noaa.oisst.v2.highres.html>) are utilized.
194 For the comparison of spatial distribution, SIC, ERA5, and OISST are interpolated to the model
195 grid.

196 3. Evaluation of updated CAPS

197 3.1. Experiment designs and methodology

198 The model domain includes 319 (449) x- (y-) grid points with a ~24 km grid spacing for
199 all model components (see Figure 2 in Y20). The WRF model uses 50 vertical levels, the
200 ROMS model uses 40 vertical levels, and the CICE model uses 7 ice layers, 1 snow layer, and
201 5 categories of sea ice thickness. The coupling frequency across all model components is 30
202 minutes. Initial and boundary conditions for the WRF and ROMS models are generated from
203 the Climate Forecast System version 2 (CFSv2, Saha et al., 2014) operational forecast archived
204 at NCEP (<http://nomads.ncep.noaa.gov/pub/data/nccf/com/cfs/prod/>). Sea ice initial conditions
205 are generated from the data assimilation described in section 2. Ensemble predictions with 8
206 members are conducted. A set of numerical experiments for the Pan-Arctic seasonal sea ice
207 prediction with different physics, starting from July 1st to October 1st for the year of 2018, has
208 been conducted. Table 2 provides the details of these experiments that allow us to examine
209 physical processes linking improved/changed physical parameterizations in the updated CAPS
210 to Arctic sea ice simulation and prediction.

211 In this study, sea ice extent is calculated as the sum of area of all grid cells with ice
212 concentration greater than 15%. Besides the total Arctic sea ice extent, we also calculate the
213 ice extent for the following subregions: 1) Beaufort and Chukchi Seas (120°W-180, 60°N-
214 80°N), 2) East Siberian and Laptev Seas (90°E-180, 60°N-80°N), and 3) Barents, Kara, and
215 Greenland Seas (30°W-90°E, 60°N-80°N). To further assess the predictive skill of Arctic sea
216 ice predictions, we show the climatology prediction (CLIM, the period of 1998-2017) and the
217 damped anomaly persistence prediction (DAMP). Following Van den Dool (2006), the DAMP
218 prediction is generated from the initial sea ice extent anomaly (relative to the 1998-2017

219 climatology) scaled by the autocorrelation and the ratio of standard deviation between different
220 lead times and initial times (see the DAMP equation in Y20).

221 In order to understand physical contributors that drive the evolution of Arctic sea ice state
222 (the standard variables of the ice concentration and thickness), the mass budget of Arctic sea
223 ice for all experiments is analyzed in this study as defined in Notz et al. (2016, Append. E),
224 including:

- 225 ● sea ice growth in supercooled open water (frazil)
- 226 ● sea ice growth at the bottom of the ice (basal growth)
- 227 ● sea ice growth due to transformation of snow to sea ice (snowice)
- 228 ● sea ice melt at the air-ice interface (top melt)
- 229 ● sea ice melt at the bottom of the ice (basal melt)
- 230 ● sea ice melt at the sides of the ice (lateral melt)
- 231 ● sea ice mass change due to dynamics-related processes (e.g. advection) (dynamics)

232 These diagnostic variables are determined by saving the ice mass tendency of above
233 processes separately every time step and integrated to output the daily-mean value.

234 **3.2. Impacts of the RAP physics in the WRF model**

235 To examine the performance of the upgrades of physical parameterization in component
236 models in CAPS one step at a time compared to its predecessor in Y20, we define the
237 Y21_CTRL experiment that uses the RAP physics in the WRF model (see Table 2 for
238 differences between Y21_CTRL and Y20_MOD). Recently, the Rapid Refresh (RAP) model,
239 a high-frequency weather prediction/assimilation modeling system operational at the National

240 Centers for Environmental Prediction (NCEP), has made some improvements in the WRF
241 model physics (Benjamin et al., 2016), including improved Grell-Freitas convection scheme
242 (GF) and Mellor-Yamada-Nakanishi-Niino planetary boundary layer scheme (MYNN). For the
243 GF scheme, the major improvements relative to the original scheme (Grell and Freitas, 2014)
244 include: 1) a beta probability density function used as the normalized mass flux profile for
245 representing height-dependent entrainment/detrainment rates within statistical-averaged deep
246 convective plumes, which is given as:

$$259 \quad Z_{u,d}(r_k) = cr_k^\alpha - (1 - r_k)^\beta - 1$$

247 where $Z_{u,d}$ is the mass flux profiles for updrafts and downdrafts, c is a normalization constant,
248 r_k is the location of the mass flux maximum, α and β determine the skewness of the beta
249 probability density function, and 2) the ECMWF approach used for momentum transport due
250 to convection (Biswas et al. 2020; Freitas et al. 2018; 2021). For the MYNN scheme, the RAP
251 model improves the mixing-length formulation, which is designed as:

$$260 \quad \frac{1}{l_m} = \frac{1}{l_s} + \frac{1}{l_t} + \frac{1}{l_b}$$

252 where l_m is the mixing length, l_s is the surface length, l_t is the turbulent length, and l_b is
253 the buoyancy length. Compared to the original scheme, the RAP model changed coefficients
254 in the formulation of l_s , l_t , and l_b for reducing the near-surface turbulent mixing, and the
255 diffusivity of the scheme. The RAP model also removes numerical deficiencies to better
256 represent subgrid-scale cloudiness (Benjamin et al. 2016, see Append. B) compared to the
257 original scheme (Nakanishi and Nino, 2009). In addition, some minor issues in the Noah land
258 surface model (Chen and Dudhia, 2001) have been fixed, including discontinuous behavior for

261 soil ice melting, negative moisture fluxes over glacial, and associated with snow melting.

262 Apparently, the above RAP physics can have influence on the behavior of simulated
263 atmospheric thermodynamics (i.e., radiation, temperature). Figure 1 and 2 show the spatial
264 distribution of the ERA5 surface downward solar and thermal radiation (SWDN and LWDN),
265 the prediction errors (ensemble mean minuses ERA5) of Y20_MOD, and the difference
266 between Y21_CTRL and Y20_MOD. For July, Y20_MOD (Fig. 1d) results in less SWDN over
267 most of ocean basins as well as Alaska and northeast US, western Siberia, and eastern Europe,
268 but more SWDN over southern and eastern Siberia compared with ERA5. For August and
269 September (Fig. 1e-f), the spatial distribution is generally similar to that of July, except that
270 eastern Siberia (less SWDN) and northern Canada (more SWDN) in August. It appears that the
271 magnitude of the prediction errors tends to decrease over the areas with large prediction errors
272 as the prediction time increases (i.e., July vs. September). Compared with Y20_MOD, the RAP
273 physics in Y21_CTRL results in large areas with smaller prediction errors in July (e.g., the
274 positive difference between Y21_CTRL and Y20_MOD reduces the negative prediction errors
275 in Y20_MOD), except the north Pacific (especially the Sea of Okhotsk) and north Canada (Fig.
276 1g). For August and September (Fig. 1h, i), encouragingly, there are more areas with smaller
277 prediction errors.

278 In contrast to SWDN, the prediction errors of LWDN in Y20_MOD have much smaller
279 magnitude (up to 100 W/m² in SWDN vs. 50 W/m² in LWDN) for the entire prediction period
280 (Fig. 2d-f). For July, Y20_MOD (Fig. 2d) simulates less LDWN over most of the model domain
281 compared with ERA5, except the Atlantic sector and north Greenland. For August, the areas

282 with negative prediction errors expand and the magnitude of prediction errors increases
283 (particularly in southeastern Siberia and northeast US) compared to that of July (Fig. 2e). For
284 September (Fig. 2f), the spatial distribution of LWDN is mostly similar to that of July, except
285 that north Canada and Canadian Archipelago show positive prediction errors. The Y21_CTRL
286 experiment with the RAP physics tends to reduce the prediction errors in Y20_MOD, especially
287 over eastern Siberia and the Atlantic sector in July to September (Fig. 2g-i). However,
288 Y21_CTRL results in larger bias in the central Northern Atlantic in August than that of
289 Y20_MOD (Fig. 2h).

290 Figure 3 shows the spatial distribution of the ERA5 2m air temperature, the prediction
291 errors of Y20_MOD, and the difference between Y21_CTRL and Y20_MOD. For Y20_MOD,
292 the predicted air temperature in July has small cold prediction errors over all ocean basins,
293 small-to-moderate cold prediction errors (~3-5 degrees) over Canada and Siberia, and
294 moderate-to-large cold prediction errors (~6-9 degrees) over eastern Europe (Fig. 3d). In
295 August (Fig. 3e), the cold prediction errors over most of the model domain are increased, in
296 particular, very large cold prediction error (over 10 degrees) is located over east Siberia. In
297 September, these cold prediction errors are decreased relatively, and some warm prediction
298 errors are found in north of Greenland (Fig. 3f). With the adaptation of the RAP physics in the
299 WRF model, Y21_CTRL, in general, produces a warmer state in most of the model domain
300 compared to that of Y20_MOD during the entire prediction period. For July (Fig. 3g), the
301 predicted air temperature is slightly warmer over the Arctic Ocean, the Pacific, and Atlantic
302 sectors, moderately warmer (~1-2 degrees) over central and eastern Siberia and Canadian

303 Archipelago, but the slightly colder over northern Canada than that of Y20_MOD. For August
304 and September (Fig. 3h), most of the model domain is warmer in Y21_CTRL than that of
305 Y20_MOD, in particular excessive cold prediction errors shown in Y20_MOD over Siberia are
306 reduced notably (~2.5-4 degrees). We notice that the RAP physics does not have significant
307 impacts on atmospheric circulations, given that Y21_CTRL and Y20_MOD have very similar
308 wind patterns (not shown).

309 Figure 4 shows the temporal evolution of the ensemble mean of the predicted Arctic sea
310 ice extent along with the NSIDC observations. In terms of total ice extent, compared to the
311 Y20_MOD experiment (blue line), the Y21_CTRL experiment (yellow line) produces ~0.5
312 million km² more ice extent at the initial. Note that the difference in the initial ice extent is
313 related to that sea ice fields in Y20_MOD and Y21_CTRL (as well as other experiments listed
314 in Table 2) are initialized based on one-month free runs (section 2), which use different physical
315 configurations listed in Table 2. These one-month free runs do not have the same evolution in
316 sea ice fields and result in different initial ice fields after data assimilation. The ice extent in
317 Y21_CTRL decreases faster than Y20_MOD during the first 2-week integration. After that,
318 they track each other closely, and predict nearly the same minimum ice extent (~4.3 million
319 km²). Like Y20_MOD, Y21_CTRL still has a delayed ice recovery in late September compared
320 to the observations. Compared with the CLIM/DAMP predictions (black dashed and dotted
321 lines), both Y20_MOD and Y21_CTRL have smaller prediction errors in August, but
322 comparable prediction errors after early September.

323 The difference in sea ice extent becomes larger at regional scales, in the East Siberian-

324 Laptev Seas, Y21_CTRL shows faster ice decline after mid-July than that of Y20_MOD,
325 whereas in the Beaufort-Chukchi Seas, Y21_CTRL predicts slower ice retreat after late July
326 than that of Y20_MOD (Fig. 4a, 4b). They are consistent with that Y21_CTRL predicts warmer
327 (relatively colder) temperature than that of Y20_MOD in the East Siberian-Laptev (Beaufort-
328 Chukchi) Seas. Both Y20_MOD and Y21_CTRL agree well with the observations in the
329 Barents-Kara-Greenland Seas (Fig. 4c). Compared with the observations, Y20_MOD performs
330 relatively better in regional ice extents than that of Y21_CTRL. Figure 5 shows the spatial
331 distribution of the NSIDC sea ice concentration and the difference between the predicted ice
332 concentration and the observations for all grid cells that the predictions and the observations
333 both have at least 15% ice concentration. The vertical and horizontal lining areas represent
334 difference of the ice edge location. Like regional ice extent shown in Figure 4, Y21_CTRL
335 predicts lower (higher) ice concentration along the East Siberian-Laptev (Beaufort-Chukchi)
336 Seas (Fig. 5e₁-e₃). Y21_CTRL also predicts less ice in the central Arctic Ocean in August and
337 September, which is consistent with warmer temperature in Y21_CTRL relative to Y20_MOD.

338 Figure 6 shows the evolution of sea ice mass budget terms of Y20_MOD and Y21_CTRL,
339 averaged with cell-area weighting over the entire model domain. During the entire prediction
340 period, most of the ice loss in Y20_MOD and Y21_CTRL are caused by basal melting. The
341 surface melting has relatively small contribution in the total ice loss and mainly occurs in July.
342 However, compared with Y20_MOD (Fig. 6a), Y21_CTRL (Fig. 6b) shows much larger
343 magnitude for basal and surface melt. In a fully coupled predictive model, the changes of sea
344 ice are determined by the fluxes from the atmosphere above and the ocean below. Associated

345 with the increased downward radiation of the above RAP physics, Y21_CTRL absorbs more
 346 shortwave radiation (SWABS, Fig. 7a) and allows more penetrating solar radiation into the
 347 upper ocean below sea ice (SWTHRU, Fig. 7b) than that of Y20_MOD, especially in July. This
 348 explains why Y21_CTRL has larger magnitude of surface and basal melting terms. Although
 349 Y21_CTRL show larger magnitude in surface and basal melting than that of Y20_MOD, the
 350 ice extent in Y21_CTRL and Y20_MOD shown in Figure 4 show similar evolution. The effect
 351 of larger surface and basal melting in Y21_CTRL is largely reflected in the ice thickness change.
 352 As shown in Figure S3, Y21_CTRL has thinner ice thickness than that of Y20_MOD, in the
 353 East Siberian-Laptev Seas in July and in the much of central Arctic Ocean in August and
 354 September.

355

356 3.3. Impacts of the tracer advection in ROMS model

357 Currently, the ROMS model that uses a generalized topography-following coordinate has
 358 two vertical coordinate transformation options:

$$363 \quad z(x, y, \sigma, t) = S(x, y, \sigma) + \zeta(x, y, t) \left[1 + \frac{S(x, y, \sigma)}{h(x, y)} \right] \quad (1)$$

$$S(x, y, \sigma) = h_c \sigma + [h(x, y) - h_c] C(\sigma)$$

359 or

$$364 \quad z(x, y, \sigma, t) = \zeta(x, y, t) + [\zeta(x, y, t) + h(x, y)] S(x, y, \sigma)$$

$$S(x, y, \sigma) = \frac{h_c \sigma + h(x, y) C(\sigma)}{h_c + h(x, y)} \quad (2)$$

360 where $S(x, y, \sigma)$ is a nonlinear vertical transformation function, $\zeta(x, y, t)$ is the free-surface,
 361 $h(x, y)$ is the unperturbed water column thickness, $C(\sigma)$ is the non-dimensional, monotonic,
 362 vertical stretching function, and h_c controls the behavior of the vertical stretching. In Y20, we

365 used the transformation 1 and the vertical stretching function introduced by Song and
366 Haidvogel (1994). However, the vertical transformation 1 has an inherent limitation for the
367 value of h_c (expected to be the thermocline depth), which must be less than or equal to the
368 minimum value in $h(x, y)$. As a result, h_c was chosen as 10 meters due to the limitation of
369 the minimum value in $h(x, y)$ in Y20. This limitation is removed with the vertical
370 transformation 2 and h_c can be any positive value. Here the Y21_VT experiment is conducted
371 to examine the impact of the vertical transformation in the ROMS model on seasonal Arctic
372 sea ice simulation and prediction, which uses the vertical transformation 2, the Shchepetkin
373 [vertical stretching function \(a function introduced in a research version of ROMS at University](#)
374 [of California, Los Angeles\)](#), and 300 meters for h_c . As shown in Supplementary Figure S4-S5,
375 compared to Y21_CTRL, Y21_VT is less sensitive to the bathymetry and its layers are more
376 evenly-distributed in the upper 300 meters. With the changes of vertical layers of the upper
377 ocean, the Y21_VT experiment has minor SST changes relative to Y21_CTRL. The simulated
378 temporal evolution of total ice extent of Y21_VT (Fig. 4, red line) resembles to that of
379 Y21_CTRL (Fig. 4, yellow line), although some differences are seen at the regional scale in
380 the areas with shallow water (e.g., East Siberian, Laptev, Barents, and Kara Seas). The
381 configuration of Y21_VT is used in the following experiments.

382 It has been recognized that the tracer advection and the vertical mixing schemes have
383 important effects on ocean and sea ice simulation (e.g., Liang and Losch, 2018; Naughten et
384 al., 2017). Here the Y21_RP experiment is designated to explore the influence of different
385 advection schemes in the ROMS model. Specifically, the tracer advection scheme is changed

386 from the Multidimensional positive definite advection transport algorithm (MPDATA;
387 Smolarkiewicz, 2006) to the third-order upwind horizontal advection (U3H; Rasch, 1994;
388 Shchepetkin, and McWilliams, 2005) and the fourth-order centered vertical advection schemes
389 (C4V; Shchepetkin, and McWilliams, 1998; 2005). The MPDATA scheme applied in
390 Y20_MOD, Y21_CTRL, and Y21_VT is a non-oscillatory scheme but a sign preserving
391 scheme (Smolarkiewicz, 2006). This means MPDATA is not suitable for tracer fields having
392 both positive and negative values (i.e., temperature with degree Celsius in the ROMS model).
393 The upwind third-order (U3H) scheme used in Y21_RP is an oscillatory scheme but it
394 significantly reduces oscillations compared to other centered schemes (e.g., Hecht et al., 2000;
395 Naughten et al., 2017) available in the ROMS model.

396 Figure 8 shows the spatial distribution of the SST changes of Y21_VT and Y21_RP
397 relative to Y21_CTRL (as well as the OISST and the difference between Y21_CTRL and
398 OISST). In general, Y21_CTRL shows cold prediction errors in the North Pacific (~2 degrees)
399 and the Atlantic (~3 degrees) compared to that of OISST in July, and these cold prediction
400 errors are enhanced as the prediction time increases (to 3-5 degrees, Fig. 8d-f). With the
401 U3H/C4V tracer advection scheme in Y21_RP, cold prediction errors shown in Y21_CTRL are
402 reduced significantly in the north Pacific and Atlantic, but SST under sea ice in much of the
403 Arctic Ocean is slightly colder than that of Y21_CTRL (Fig. 8j-l).

404 Y21_RP (Fig. 4, green line) shows comparable temporal evolution of the ice extent as
405 Y21_CTRL (as well as Y21_VT) until near the end of July. After that, the ice melting slows
406 down (closer to the observations) and the ice extent begins to recover earlier (after the first

407 week of September) in Y21_RP compared to that of Y21_CTRL. This leads to much smaller
408 prediction error in seasonal minimum ice extent relative to the observation. Y21_RP also shows
409 better predictive skill after late August compared with the CLIM/DAMP predictions (black
410 dashed and dotted lines). This suggests the delayed ice recovery in late September shown in
411 Y20_MOD, Y21_CTRL and Y21_VT is in part due to the choice of ocean advection and
412 vertical mixing schemes, which change the behavior of ocean state. At the regional scale, the
413 slower ice decline after July and earlier recovery of the ice extent in September mainly occur
414 in the Beaufort-Chukchi and Barents-Kara-Greenland Seas compared to that of Y21_CTRL
415 (Fig. 4a, c). With U3H/C4V scheme, the Y21_RP experiment simulates higher sea ice
416 concentration than that of Y21_VT (Fig. 5f₁-f₃). For September, the Y21_RP experiment better
417 predicts the ice edge location in the Atlantic sector of the Arctic (i.e., smaller areas with
418 horizontal/vertical lining) compared to the experiments described above (not shown).

419 Figure 9 shows the evolution of sea ice mass budget terms of Y21_VT and Y21_RP.
420 Relative to Y21_VT, Y21_RP (with U3H/C4V scheme) results in increased frazil ice formation
421 in July, which is partly compensated by increased surface melting. Y21_RP also leads to
422 increased basal growth in mid- and late September (Fig. 9a, b).

423 Figure 10 shows the difference in the vertical profile of ocean temperature and salinity in
424 the upper 150 m averaged for the central Arctic Ocean between Y21_RP and Y21_VT. The
425 ocean temperature in the surface layer of Y21_RP is slightly colder during the prediction period
426 compared to that of Y21_VT (Fig. 10a), especially in August and September. Moreover, the
427 water in the surface layer (0-20 m) of Y21_RP is fresher than that of Y21_VT (Fig. 10b). It

428 reduces the freezing temperature and favours frazil ice formation. In CAPS, frazil ice formation
429 is determined by the freezing potential, which is the vertical integral of the difference between
430 temperature in upper ocean layer and the freezing temperature in the upper 5 m-layer. The
431 temperature of supercooled water is adjusted based on the freezing potential to form new ice
432 and rejects brine into the ocean that leads to saltier water between 20-50 m in Figure 10. It
433 should be noted that the increased frazil ice formation in July in Y21_RP might be also the
434 results of model adjustment and/or numerical error. The oscillatory behavior of U3H scheme
435 can make the temperature fall below the freezing point and then instantaneously forms new ice
436 (as well as temperature/salinity adjustments).

437 **3.4. Impacts of sea ice thermodynamics in the CICE model**

438 In Y20, we used sea ice thermodynamics introduced by Bitz and Lipscomb (1999;
439 hereafter BL99) as the setup of CAPS, which assumes a fixed vertical salinity profile based on
440 observations. The new CICE model includes a MUSHY-layer ice thermodynamics introduced
441 by Turner et al. (2013), which simulates vertically and time-varying prognostic salinity and
442 associated effects on thermodynamic properties of sea ice. In the Y21_MUSHY experiment,
443 we change the ice thermodynamics from BL99 to MUSHY (Table 2) to examine whether
444 improved ice thermodynamics has noticeable influence on Arctic sea ice simulation and
445 prediction at seasonal timescale. Compared to Y21_RP, Y21_MUSHY (Fig. 4, pink line)
446 produces very similar evolution of total ice extent. However, it simulates relatively larger ice
447 extent near the end of September, which is also reflected by the basin-wide increased ice cover
448 shown in Figure 5h3. At the regional scale, compared to Y21_RP, Y21_MUSHY predicts less

449 ice in August in the Beaufort-Chukchi. The opposite is the case for the East Siberian-Laptev
450 Seas (Fig. 4a, b).

451 Figure 11 shows the difference of the ensemble mean of the predicted ice thickness
452 between Y21_MUSHY and Y21_RP. Compared with Y21_RP, Y21_MUSHY simulates
453 thicker ice (from ~0.2m in July to over 0.4m in September) extending from the Canadian Arctic,
454 through the central Arctic Ocean, to the Laptev Sea (Fig. 11a-c). This seems to be consistent
455 with previous studies, which show that the Mushy-layer thermodynamics simulates thicker ice
456 than BL99 thermodynamics in both standalone CICE (Turner and Hunke, 2015) and the fully-
457 coupled (Bailey et al., 2020), but Y21_MUSHY shows thinner ice (~0.2m) in an arc extending
458 from north of Alaska to north of eastern Siberia compared to Bailey et al. (2020). Note that
459 Y21_MUSHY focuses the effects of Mushy-thermodynamics on seasonal timescale while the
460 results in Bailey et al. (2020) are based on 50-year simulations.

461 Compared to Y21_RP, the mass budget of Y21_MUSHY (Fig. S6) shows that both surface
462 melting and frazil ice formation terms are increased. This compensation between surface
463 melting and frazil ice formation from the Mushy-layer thermodynamics in CAPS leads to
464 relatively unchanged total ice extent between Y21_MUSHY and Y21_RP (Fig. 4 green and
465 pink lines).

466

467 **4. Prediction skill of CAPS at longer timescale**

468 The design of Arctic sea ice prediction experiments described above follow the protocol
469 of the Sea Ice Prediction Network ([SIPN](#)), in which the outlook start from June 1st, July 1st, and

470 August 1st to predict seasonal minimum of the ice extent in September. It is not clear that how
471 predictive skills of dynamical models participating in SIPN may change for longer period. Here
472 we conduct two more experiments to investigate the predictive capability of CAPS beyond the
473 SIPN prediction period. For the prediction experiments discussed above, we use a simple
474 approach to merge CryoSat-2 and SMOS ice thickness by replacing ice thickness less than 1m
475 in CryoSat-2 data with SMOS data for ice thickness assimilation. Ricker et al. (2017) presented
476 a new ice thickness product (CS2SMOS) based on the optimal interpolation to statistically
477 merge CryoSat-2 and SMOS data. Here we utilize the configuration of Y21_RP but use
478 CS2SMOS SIT for the assimilation (Y21_SIT; Table 2). The predicted total ice extent is almost
479 identical to Y21_RP in July but slightly larger total extent after July than that of Y21_RP (not
480 shown). The configuration of Y21_SIT is used in the following experiments. Taking advantage
481 of the entire prediction period provided by CFS forecasts (7 months), the Y21_EXT-7
482 experiment is designed to extend the prediction period to the end of January next year (Table
483 2). Figure 12 shows the temporal evolution of the ensemble mean of the predicted total Arctic
484 sea ice extent (as well as regional ice extent) for Y21_EXT-7. Total ice extent of Y21_EXT-7
485 exhibits reasonable evolution in terms of seasonal minimum and timing of recovery compared
486 with the observations until late November. Y21_EXT-7 also performs better than that of the
487 CLIM/DAMP predictions (black dashed and dotted lines) until mid-to-late November. After
488 that, Y21_EXT-7 overestimates total ice extent relative to the observations, and such
489 overestimation is largely contributed by more extensive sea ice in the Barents-Kara-Greenland
490 Seas (Fig. 12c), which is a result of a sharp increase in the basal growth term after mid-to-late

512 November (not shown).

513 **5. Conclusions and Discussions**

514 This paper presents and evaluates the updated Coupled Arctic Prediction System (CAPS)
515 designated for Arctic sea ice prediction through a case study for the year of 2018. A set of Pan-
516 Arctic prediction experiments with improved/changed physical parameterizations as well as
517 different configurations starting from July 1st to the end of September are performed for 2018
518 to assess their impacts of the updated CAPS on the predictive skill of Arctic sea ice at seasonal
519 timescale. Specifically, we focus on the Rapid Refresh (RAP) physics in the WRF model, the
520 oceanic tracer advection scheme in the ROMS model, sea ice thermodynamics in the CICE
521 model, and investigate physical [processes](#) linking them to Arctic sea ice simulation and
522 prediction.

523 The results show that the updated CAPS with improved physical parameterizations can
524 better predict the evolution of total ice extent compared with its predecessor described in Yang
525 et al. (2020), though the predictions exhibit some prediction errors in regional ice extent. The
526 key improvements of WRF, including cumulus, boundary layer, and land surface schemes,
527 result in improved simulations in downward radiative fluxes and near surface air temperature.
528 These improvements mainly influence the predicted ice thickness instead of total ice extent.
529 The difference in the predicted ice thickness can have potential impacts on the icebreakers
530 planning their routes across the ice-covered regions. The major changes of ROMS, including
531 tracer advection and vertical mixing schemes, reduces the prediction [errors](#) in sea surface
532 temperature and changes ocean temperature and salinity structure in the surface layer, leading

设置了格

533 to improved evolution of the predicted total ice extent (particularly correcting the late ice
534 recovery issue in the previous CAPS). The changes of CICE, including improved ice
535 thermodynamics, have noticeable influences on the predicted ice thickness.

536 We demonstrate that CAPS can remain skillful beyond the designated period of Sea Ice
537 Prediction Network (SIPN), which has potential values for stakeholders to make decisions
538 regarding the socioeconomical activities in the Arctic. Although CAPS shows extended
539 predictive skill to the freeze-up period, the prediction produces extensive ice through the basal
540 growth near the end of prediction. The excessive basal growth may be partly due to that the
541 bias of the CFS data propagates into the model domain through lateral boundary conditions
542 and its accumulated effect influences Arctic sea ice simulation during the freeze-up period.

543 Keen et al. (2021) analyzed the Arctic mass budget of 15 models participated in the
544 Coupled Model Intercomparison Project Phase 6 (CMIP6). We notice that, first, the top melting
545 and the basal melting terms in CMIP6 models have comparable contributions in July while the
546 top melting term only has ~50% contribution relative to the basal melting term in CAPS. The
547 updated CAPS with the RAP physics improves the performance of shortwave/longwave
548 radiation at the surface (Fig. 1 and Fig. 2). The net flux at the ice surface, however, may still
549 be underestimated in the updated CAPS. Besides, the surface property of sea ice (i.e., the
550 amount of melt ponds, bare ice, and snow) is a factor that influences surface albedo and thus
551 the absorbed shortwave radiation (e.g., Nicolaus et al., 2012; Nicolaus and Katlein, 2013). The
552 prediction experiments starting at July 1st in this study do not consider the initialization of melt
553 ponds (i.e., zero melt pond coverage at the initial). However, melt ponds start to develop in

554 early May based on the satellite observations (e.g., Liu et al., 2015, Fig. 1). The initialization
555 of melt pond based on the observations (e.g., Ding et al., 2020) in CAPS is a direction to
556 improve the representation of the ice surface properties. Second, the mass budget analysis by
557 both Keen et al. (2021) and this study show that the contribution of lateral melting term is
558 relatively small, which might be due to that CMIP6 models and CAPS assume constant floe-
559 size (i.e., 300 meters in CICE), which is a critical value to determine the strength of lateral
560 melting (e.g., Horvat et al., 2016; Steele, 1992). Recently, several studies have proposed floe
561 size distribution models (e.g., Bateson et al., 2020; Bennetts et al., 2017; Boutin et al., 2020;
562 Horvat and Tziperman, 2015; Roach et al., 2018, 2019; Zhang et al., 2015, 2016). Incorporating
563 floe size distribution model in CAPS and understanding its impacts on seasonal Arctic sea ice
564 prediction will be a future direction of developing CAPS. Lastly, the prediction experiments
565 with the upwind advection scheme (i.e., Y21_RP, Y21_EXT-7) shows spurious large frazil ice
566 formation, particularly in July, which is different from the analysis shown in Keen et al. (2021).
567 An approach for reducing spurious frazil ice formation is proposed by Naughten et al. (2017)
568 that they implemented upwind [flux](#) limiter (Leonard and Mokhtari, 1990) to the U3H scheme
569 to further reduce the oscillations. Naughten et al. (2018) also suggested that the oscillatory
570 behaviors can be smoothed out by applying the Akima fourth-order tracer advection scheme
571 combined with Laplacian horizontal diffusion at a level strong enough. Beside of the oscillatory
572 behaviors of advection scheme, the ice-ocean heat flux [may](#) also play a role in the spurious
573 frazil ice formation. As discussed in section 3.3, the freezing/melting potential not only
574 determines the amount of newly-formed ice, but also limits the amount of energy that can be

575 extracted from the ocean surface layer to melt sea ice. This implies that the ocean surface layer
576 will be close to the freezing temperature if the ice-ocean heat fluxes reach the limit imposed by
577 the melting potential. Shi et al. (2021) discussed the impacts of different ice-ocean heat flux
578 parametrizations on sea ice simulations. Their results suggest that Arctic sea ice will be thicker
579 and ocean temperature will warmer beneath high-concentration ice with a complex approach
580 proposed by Schmidt et al. (2004) that limits melt rates (heat fluxes) of sea ice through
581 considering a fresh water layer underlying sea ice. The warmer ocean temperature under sea
582 ice with a more complex approach in parameterizing ice-ocean heat flux may be the solution
583 to reduce the occurrence of local temperature falling below freezing temperature with
584 oscillatory advection schemes.

585 Based on the prediction experiments discussed in this paper, the configuration with the
586 RAP physics, the U3H/C4V ocean advection, BL99 ice thermodynamics, and CS2SMOS ice
587 thickness assimilation (Table 2, Y21_SIT) is assigned as the finalized CAPS version 1.0.
588 Improving the representation of physical processes in CAPS version 1.0 for further reducing
589 the model bias will remain the main focus for the development of CAPS. Since CAPS is a
590 regional modeling system, it relies on the forecasts from global climate models as initial and
591 lateral boundary conditions. That is, biases existed in GCM simulations (here the CFS forecast)
592 can be propagated into and affect the entire area-limited domain (e.g., Bruyère et al., 2014;
593 Rocheta et al., 2020; Wu et al., 2005). This issue can be a potential source that influences the
594 predictive capability of CAPS for longer timescales. Studies have applied bias correction
595 techniques with different complexities for improving the performance of regional modeling

596 system (e.g., Bruyère et al., 2014; Colette et al., 2012; Rocheta et al., 2017, 2020). Further
597 investigation is needed to address biases inherited from GCM predictions through lateral
598 boundaries for improving the predictive capability of CAPS.
599

600 Code and data availability: The COAWST and CICE models are open source and can be
601 downloaded from their developers at <https://github.com/jcwarner-usgs/COAWST> and
602 <https://github.com/CICE-Consortium/CICE>, respectively. PDAF can be obtained from
603 <https://pdaf.awi.de/trac/wiki>. CAPS v1.0 described in this paper is permanently archived at
604 <https://doi.org/10.5281/zenodo.5034971>. The prediction data analyzed in this paper can be
605 accessed from <https://doi.org/10.5281/zenodo.4911415>.

606

607 Author contributions: CYY and JL designed the model experiments, developed the
608 updated CAPS model, and wrote the manuscript, CYY conducted the prediction experiments
609 and analyzed the results. DC provided constructive feedback on the manuscript.

610

611 Competing interests: The authors declare that they have no conflict of interest.

612

613 Acknowledgements: This research is supported by the National [Key R&D Program of](#)
614 [China \(2018YFA0605901\)](#), the [National](#) Natural Science Foundation of China (42006188 [and](#)
615 [41922044](#)), [_____](#) and the Innovation Group Project of Southern Marine Science and
616 Engineering Guangdong Laboratory (Zhuhai) (311021008). The authors also acknowledge the
617 National Centers for Environmental Prediction for providing CFS seasonal forecasts, the
618 University of Hamburg for distributing the SMOS sea ice thickness data, the Alfred-Wegener-
619 Institut, Helmholtz Zentrum für Polar- und Meeresforschung for providing the CryoSat-2 sea
620 ice thickness data and CS2SMOS data, the Polar Science Center for distributing the PIOMAS
621 ice thickness data, the National Snow and Ice Data Center for providing the SSMIS sea ice
622 concentration data, the European Centre for Medium-Range Weather Forecasts for distributing
623 the ERA5 reanalysis, and the National Oceanic and Atmospheric Administration for providing
624 the OI sea surface temperature.

625 **6. References**

- 626 Aagaard, K.: A synthesis of the Arctic Ocean circulation. *Rapp. P.-V. Reun.- Cons. Int. Explor.*
627 *Mer*, 188, 11–22, 1989.
- 628 Bailey, D. A., Holland, M. M., DuVivier, A. K., Hunke, E. C., and Turner, A. K.: Impact of a
629 new sea ice thermodynamic formulation in the CESM2 sea ice component. *Journal of*
630 *Advances in Modeling Earth Systems*, 12, e2020MS002154.
631 <https://doi.org/10.1029/2020MS002154>, 2020.
- 632 Bateson, A. W., Feltham, D. L., Schröder, D., Hosekova, L., Ridley, J. K., and Aksenov, Y.:
633 Impact of sea ice floe size distribution on seasonal fragmentation and melt of Arctic sea
634 ice, *The Cryosphere*, 14, 403–428, <https://doi.org/10.5194/tc-14-403-2020>, 2020.
- 635 Bitz, C. M. and Lipscomb, W. H.: An energy-conserving thermodynamic sea ice model for
636 climate study. *J. Geophys. Res.-Oceans*, 104, 15669–15677, 1999.
- 637 Benjamin, S. G., Weygandt, S. S., Brown, J. M., Hu, M., Alexander, C. R., Smirnova, T. G.
638 and Manikin, G. S.: A North American hourly assimilation and model forecast cycle: the
639 Rapid Refresh. *Monthly Weather Review*, 144, 1669–1694.
640 <https://doi.org/10.1175/MWR-D-15-0242.1>, 2016.
- 641 Bennetts, L. G., O'Farrell, S., and Uotila, P.: Brief communication: Impacts of ocean-wave-
642 induced breakup of Antarctic sea ice via thermodynamics in a stand-alone version of the
643 CICE sea-ice model, *The Cryosphere*, 11, 1035–1040, [https://doi.org/10.5194/tc-11-](https://doi.org/10.5194/tc-11-1035-2017)
644 [1035-2017](https://doi.org/10.5194/tc-11-1035-2017), 2017.
- 645 Biswas, M. K., Zhang, J. A., Grell, E., Kalina, E., Newman, K., Bernardet, L., Carson, L.,
646 Frimel, J., and Grell, G.: Evaluation of the Grell–Freitas Convective Scheme in the
647 Hurricane Weather Research and Forecasting (HWRF) Model, *Weather and Forecasting*,
648 35(3), 1017–1033, 2020.
- 649 Blanchard-Wrigglesworth, E., Bitz, C., and Holland, M.: Influence of initial conditions and
650 climate forcing on predicting Arctic sea ice. *Geophysical Research Letters*, 38, L18503.
651 <https://doi.org/10.1029/2011GL048807>, 2011.

652 Blanchard-Wrigglesworth, E., and Bushuk, M.: Robustness of Arctic sea-ice predictability in
653 GCMs. *Climate Dynamics*, 52, 5555–5566, 2018.

654 Blanchard-Wrigglesworth, E., Cullather, R., Wang, W., Zhang, J., and Bitz, C. M.: Model
655 forecast skill and sensitivity to initial conditions in the seasonal sea ice outlook.
656 *Geophysical Research Letters*, 42, 8042–8048. <https://doi.org/10.1002/2015GL065860>,
657 2015.

658 Boutin, G., Lique, C., Ardhuin, F., Rousset, C., Talandier, C., Accensi, M., and Girard-Ardhuin,
659 F.: Towards a coupled model to investigate wave–sea ice interactions in the Arctic
660 marginal ice zone, *The Cryosphere*, 14, 709–735, [https://doi.org/10.5194/tc-14-709-](https://doi.org/10.5194/tc-14-709-2020)
661 2020, 2020.

662 Briegleb, B. P. and Light, B.: A Delta-Eddington multiple scattering parameterization for solar
663 radiation in the sea ice component of the Community Climate System Model. NCAR
664 Tech. Note NCAR/TN-472+STR, National Center for Atmospheric Research, 2007.

665 Bruyère, C. L., Done, J. M., Holland, G. J., and Fredrick, S.: Bias corrections of global models
666 for regional climate simulations of high-impact weather. *Clim Dyn* 43, 1847–1856
667 (2014). <https://doi.org/10.1007/s00382-013-2011-6>, 2014.

668 Carmack, E., Polyakov, I., Padman, L., Fer, I., Hunke, E., Hutchings, J., Jackson, J., Kelley,
669 D., Kwok, R., Layton, C., Melling, H., Perovich, D., Persson, O., Ruddick, B.,
670 Timmermans, M.-L., Toole, J., Ross, T., Vavrus, S., and Winsor, P.: Toward Quantifying
671 the Increasing Role of Oceanic Heat in Sea Ice Loss in the New Arctic. *Bulletin of the*
672 *American Meteorological Society* 96, 12, 2079–2105, [https://doi.org/10.1175/BAMS-D-](https://doi.org/10.1175/BAMS-D-13-00177.1)
673 [13-00177.1](https://doi.org/10.1175/BAMS-D-13-00177.1), 2015.

674 Cavalieri, D. J., Parkinson, C. L., Gloersen, P., and Zwally, H. J.: updated yearly. Sea Ice
675 Concentrations from Nimbus-7 SMMR and DMSP SSM/I-SSMIS Passive Microwave
676 Data, Version 1. Boulder, Colorado USA. NASA National Snow and Ice Data Center
677 Distributed Active Archive Center. <https://doi.org/10.5067/8GQ8LZQVLOVL>, 1996.

678 Chen, F. and Dudhia, J.: Coupling an advanced land surface–hydrology model with the Penn
679 State–NCAR MM5 modeling system. Part I: Model implementation and sensitivity. *Mon.*
680 *Wea. Rev.*, 129, 569–585, 2001.

681 Chevallier, M., Salas y Mélia, D., Voldoire, A., Déqué, M., and Garric, G.: Seasonal forecasts
682 of the pan-Arctic sea ice extent using a GCM-based seasonal prediction system. *Journal*
683 *of Climate*, 26(16), 6092–6104, 2013.

684 Colette, A., Vautard, R., and Vrac, M.: Regional climate downscaling with prior statistical
685 correction of the global climate forcing, *Geophys. Res. Lett.*, 39, L13707,
686 <https://doi.org/10.1029/2012GL052258>, 2012.

687 Day, J. J., Tietsche, S., Collins, M., Goessling, H. F., Guemas, V., Guillory, A., et al.: The
688 Arctic predictability and prediction on seasonal-to-interannual timescales (apposite) data
689 set version 1. *Geoscientific Model Development*, 9, 2255–2270, 2016.

690 Ding, Y., Cheng, X., Liu, J., Hui, F., Wang, Z., and Chen, S.: Retrieval of Melt Pond Fraction
691 over Arctic Sea Ice during 2000–2019 Using an Ensemble-Based Deep Neural Network.
692 *Remote Sensing*. 12(17):2746. <https://doi.org/10.3390/rs12172746>, 2020

693 DuVivier, A. K., Holland, M. M., Landrum, L., Singh, H. A., Bailey, D. A., and Maroon, E.
694 A.: Impacts of sea ice mushy thermodynamics in the Antarctic on the coupled Earth
695 system. *Geophysical Research Letters*, 48, e2021GL094287.
696 <https://doi.org/10.1029/2021GL094287>, 2021.

697 Fer, I.: Near-inertial mixing in the central Arctic Ocean. *J. Phys. Oceanogr.*, 44, 2031–2049,
698 <https://doi.org/10.1175/JPO-D-13-0133.1>, 2014.

699 Fetterer, F., Knowles, K., Meier, W. N., Savoie, M., and Windnagel, A. K.: updated daily. Sea
700 Ice Index, Version 3. Boulder, Colorado USA. NSIDC: National Snow and Ice Data
701 Center. <https://doi.org/10.7265/N5K072F8>, 2017.

702 Freitas, S. R., Grell, G. A., Molod, A., Thompson, M. A., Putman, W. M., Santos e Silva, C.
703 M. and Souza, E. P.: Assessing the Grell–Freitas convection parameterization in the

704 NASA GEOS modeling system. *J. Adv. Model. Earth Syst.*, 10, 1266–1289,
705 <https://doi.org/10.1029/2017MS001251>, 2018.

706 Freitas, S. R., Grell, G. A., and Li, H.: The Grell–Freitas (GF) convection parameterization:
707 recent developments, extensions, and applications, *Geosci. Model Dev.*, 14, 5393–5411,
708 <https://doi.org/10.5194/gmd-14-5393-2021>, 2021.

709 Germe, A., Chevallier, M., y Mélia, D. S., Sanchez-Gomez, E., and Cassou, C.: Interannual
710 predictability of Arctic sea ice in a global climate model: Regional contrasts and
711 temporal evolution. *Climate Dynamics*, 43(9-10), 2519–2538, 2014.

712 Grell, G. A., and Freitas, S.: A scale and aerosol aware stochastic convective parameterization
713 for weather and air quality modeling. *Atmos. Chem. Phys.*, 14, 5233–5250,
714 <https://doi.org/10.5194/acp-14-5233-2014>, 2014.

715 Guemas, V., Blanchard-Wrigglesworth, E., Chevallier, M., Day, J. J., Déqué, M., Doblus-
716 Reyes, F. J., et al.: A review on Arctic sea-ice predictability and prediction on seasonal
717 to decadal time-scales. *Quarterly Journal of the Royal Meteorological Society*, 142(695),
718 546–561, 2016.

719 Haidvogel, D. B., Arango, H., Budgell, W. P., Cornuelle, B. D., Curchitser, E., Di Lorenzo, E.,
720 et al.: Ocean forecasting in terrain-following coordinates: Formulation and skill
721 assessment of the Regional Ocean Modeling System, *Journal of Computational Physics*,
722 227, 3595–3624, 2008.

723 Hecht, M. W., Wingate, B. A., and Kassis, P.: A better, more discriminating test problem for
724 ocean tracer transport. *Ocean Modell.* 2 (1–2), 1–15. [https://doi.org/10.1016/S1463-50](https://doi.org/10.1016/S1463-5003(00)00004-4)
725 [03\(00\)00004-4](https://doi.org/10.1016/S1463-5003(00)00004-4), 2000.

726 Hersbach, H., Bell, B., Berrisford, P., et al.: The ERA5 global reanalysis. *Quarterly Journal of*
727 *the Royal Meteorological Society*, 146, 1999–2049. <https://doi.org/10.1002/qj.3803>,
728 2020.

729 Horvat, C., and Tziperman, E.: A prognostic model of the sea-ice floe size and thickness
730 distribution. *Cryosphere* 9, 2119–2134, 2015.

731 Horvat, C., Tziperman, E., and Campin, J.-M.: Interaction of sea ice floe size, ocean eddies,
732 and sea ice melting. *Geophysical Research Letters*, 43, 8083–8090.
733 <https://doi.org/10.1002/2016GL069742>, 2016.

734 Huang, Y., Chou, G., Xie, Y., & Soular, N.: Radiative control of the interannual variability
735 of Arctic sea ice. *Geophysical Research Letters*, 46, 9899– 9908.
736 <https://doi.org/10.1029/2019GL084204>, 2019.

737 Itoh, M., Nishino, S., Kawaguchi, Y., and Kikuchi, T.: Barrow Canyon volume, heat, and
738 freshwater fluxes revealed by long-term mooring observations between 2000 and 2008.
739 *J. Geophys. Res. Oceans*, 118, 4363–4379, <https://doi.org/10.1002/jgrc.20290>, 2013.

740 Jung, T., Gordon, N.D., Bauer, P., Bromwich, D.H., Chevallier, M., Day, J.J., Dawson, J.,
741 Doblas-Reyes, F., Fairall, C., Goessling, H.F., Holland, M., Inoue, J., Iversen, T., Klebe,
742 S., Lemke, P., Losch, M., Makshtas, A., Mills, B., Nurmi, P., Perovich, D., Reid, P.,
743 Renfrew, I.A., Smith, G., Svensson, G., Tolstykh, M., and Yang, Q.: Advancing Polar
744 Prediction Capabilities on Daily to Seasonal Time Scales. *Bulletin of the American*
745 *Meteorological Society*. <https://doi.org/10.1175/BAMS-D-14-00246.1>, 2016.

746 Kaleschke, L., Tian-Kunze, X., Maaß, N., Mäkynen, M., and Drusch, M.: Sea ice thickness
747 retrieval from SMOS brightness temperatures during the Arctic freeze-up period.
748 *Geophys. Res. Lett.*, L05501, <https://doi.org/10.1029/2012GL050916>, 2012.

749 Kapsch, M., Graversen, R. G., Tjernström, M., and Bintanja, R.: The Effect of Downwelling
750 Longwave and Shortwave Radiation on Arctic Summer Sea Ice. *Journal of Climate* 29,
751 3, 1143-1159, <https://doi.org/10.1175/JCLI-D-15-0238.1>, 2016.

752 Kay, J. E., L’Ecuyer, T., Gettelman, A., Stephens, G., and O’Dell, C.: The contribution of cloud
753 and radiation anomalies to the 2007 Arctic sea ice extent minimum, *Geophys. Res. Lett.*,
754 35, L08503, doi:10.1029/2008GL033451, 2008.

755 Keen, A., Blockley, E., Bailey, D. A., Boldingh Debernard, J., Bushuk, M., Delhaye, S.,
756 Docquier, D., Feltham, D., Massonnet, F., O’Farrell, S., Ponsoni, L., Rodriguez, J. M.,
757 Schroeder, D., Swart, N., Toyoda, T., Tsujino, H., Vancoppenolle, M., and Wyser, K.:

758 An inter-comparison of the mass budget of the Arctic sea ice in CMIP6 models, *The*
759 *Cryosphere*, 15, 951–982, <https://doi.org/10.5194/tc-15-951-2021>, 2021.

760 Kirkman, C. H., IV, and Bitz, C. M.: The Effect of the Sea Ice Freshwater Flux on Southern
761 Ocean Temperatures in CCSM3: Deep-Ocean Warming and Delayed Surface Warming.
762 *Journal of Climate* 24, 9, 2224–2237, <https://doi.org/10.1175/2010JCLI3625.1>, 2011.

763 Kwok, R.: Arctic sea ice thickness, volume, and multiyear ice coverage: Losses and coupled
764 variability (1958–2018). *Environmental Research Letters*, 13(10), 105005, 2018

765 Laxon, S., Giles, K. A., Ridout, A. L., Wingham, D. J., Willatt, R., Cullen, R., Kwok, R.,
766 Schweiger, A., Zhang, J., Haas, C., Hendricks, S., Krishfield, R., Kurtz, N., Farrell, S.,
767 and Davidson, M.: CryoSat-2 estimates of Arctic sea ice thickness and volume, *Geophys.*
768 *Res. Lett.*, 40, <https://doi.org/10.1002/grl.50193>, 2013.

769 Lemieux, J. F., Dupont, F., Blain, P., Roy, F., Smith, G. C., and Flato, G. M.: Improving the
770 simulation of landfast ice by combining tensile strength and a parameterization for
771 grounded ridges. *J. Geophys. Res. Oceans*, 121:7354–7368,
772 <http://dx.doi.org/10.1002/2016JC012006>, 2016.

773 Leonard, B., Mokhtari, S.: ULTRA-SHARP Non oscillatory Convection Schemes for High-
774 Speed Steady Multidimensional Flow. Technical Report. NASA, 1990.

775 Liang, X., and Losch, M.: On the effects of increased vertical mixing on the Arctic Ocean and
776 sea ice. *Journal of Geophysical Research: Oceans*, 123, 9266– 9282.
777 <https://doi.org/10.1029/2018JC014303>, 2018.

778 Liu, J., Song, M., Horton, R., and Hu, Y.: Revisiting the potential of melt pond fraction as a
779 predictor for the seasonal Arctic sea ice minimum. *Environmental Research Letters*, 10,
780 054017. <https://doi.org/10.1088/1748-9326/10/5/054017>, 2015.

781 Liu, J., Chen, Z., Hu, Y., Zhang, Y., Ding, Y., Cheng, X., et al.: Towards reliable arctic sea ice
782 prediction using multivariate data assimilation. *Science Bulletin*, 64(1), 63–72, 2019.

783 Merryfield, W., Lee, W.-S., Wang, W., Chen, M., and Kumar, A.: Multi-system seasonal
784 predictions of Arctic sea ice. *Geophysical Research Letters*, 40, 1551–1556.
785 <https://doi.org/10.1002/grl.50317>, 2013.

786 Mallett, R. D. C., Stroeve, J. C., Cornish, S. B. Crawford, A. D., Lukovich, J. V., Serreze, M.
787 C., Barrett, A. P., Meier, W. N., Heorton, H. D. B. S., and Tsamados, M.: Record winter
788 winds in 2020/21 drove exceptional Arctic sea ice transport. *Commun Earth Environ* 2,
789 149, <https://doi.org/10.1038/s43247-021-00221-8>, 2021.

790 Maslanik, J. and Stroeve, J.: Near-Real-Time DMSP SSMIS Daily Polar Gridded Sea Ice
791 Concentrations, Version 1. Boulder, Colorado USA. NASA National Snow and Ice Data
792 Center Distributed Active Archive Center. <https://doi.org/10.5067/U8C09DWVX9LM>,
793 1999.

794 McLaughlin, F. A., Carmack, E. C., Williams, W. J., Zimmerman, S., Shimada, K., and Itoh,
795 M.: Joint effects of boundary currents and thermohaline intrusions on the warming of
796 Atlantic water in the Canada Basin, 1993–2007. *J. Geophys. Res.*, 114, C00A12,
797 <https://doi.org/10.1029/2008JC005001>, 2009.

798 Meehl, G.A., Stocker, T. F., Collins, W. D., et al.: Global Climate Projections. In: *Climate*
799 *Change 2007: The Physical Science Basis. Contribution of Working Group I to the*
800 *Fourth Assessment Report of the Intergovernmental Panel on Climate Change* [Solomon,
801 S., D. Qin, M. Manning, Z. Chen, M. Marquis, K.B. Averyt, M. Tignor and H.L. Miller
802 (eds.)]. Cambridge University Press, Cambridge, United Kingdom and New York, NY,
803 USA, 2007.

804 Msadek, R., Vecchi, G., Winton, M., and Gudgel, R.: Importance of initial conditions in
805 seasonal predictions of Arctic sea ice extent. *Geophysical Research Letters*, 41, 5208–
806 5215. <https://doi.org/10.1002/2014GL060799>, 2014.

807 Nakanishi, M., and Niino., H.: Development of an improved turbulence closure model for the
808 atmospheric boundary layer. *J. Meteor. Soc. Japan*, 87, 895–912,
809 <https://doi.org/10.2151/jmsj.87.895>, 2009.

810 Naughten, K. A., Galton-Fenzi, B. K., Meissner, K. J., England, M. H., Brassington, G. B.,
811 Colberg, F., Hattermann, T., and Debernard, J. B.: Spurious sea ice formation caused by
812 oscillatory ocean tracer advection schemes. *Ocean Model.*, 116, 108–117, 2017.

813 Naughten, K. A., Meissner, K. J., Galton-Fenzi, B. K., England, M. H., Timmermann, R.,
814 Hellmer, H. H., Hattermann, T., and Debernard, J. B.: Intercomparison of Antarctic ice-
815 shelf, ocean, and sea-ice interactions simulated by MetROMS-iceshelf and FESOM 1.4.
816 *Geosci. Model. Dev.*, 11, 1257–1292, 2018

817 Nerger, L., and Hiller, W.: Software for Ensemble-based Data Assimilation Systems -
818 Implementation Strategies and Scalability. *Computers and Geosciences*, 55, 110-118.
819 <https://doi.org/10.1016/j.cageo.2012.03.026>, 2013.

820 Nerger, L., Janjić, T., Schröter, J. and Hiller, W.: A unification of ensemble square root Kalman
821 filters. *Monthly Weather Review*, 140, 2335-2345. [https://doi.org/10.1175/MWR-D-11-](https://doi.org/10.1175/MWR-D-11-00102.1)
822 [00102.1](https://doi.org/10.1175/MWR-D-11-00102.1), 2012.

823 Newton, R., Pfirman, S., Schlosser, P., Tremblay, B., Murray, M. and Pomerance, R.: White
824 Arctic vs. Blue Arctic: A case study of diverging stakeholder responses to environmental
825 change. *Earth's Future*, 4: 396-405. <https://doi.org/10.1002/2016EF000356>, 2016.

826 Nicolaus M., Katlein, C., Maslanik, J., and Hendricks, S.: Changes in Arctic sea ice result in
827 increasing light transmittance and absorption. *Geophysical Research Letters*, 39, L24501.
828 <https://doi.org/10.1029/2012GL053738>, 2012

829 Nicolaus M., and Katlein, C.: Mapping radiation transfer through sea ice using a remotely
830 operated vehicle (ROV). *The Cryosphere*, 7, 763-77. [https://doi.org/10.5194/tc-7-763-](https://doi.org/10.5194/tc-7-763-2013)
831 [2013](https://doi.org/10.5194/tc-7-763-2013), 2013.

832 Notz, D., Jahn, A., Holland, M., Hunke, E., Massonnet, F., Stroeve, J., Tremblay, B., and
833 Vancoppenolle, M.: The CMIP6 Sea-Ice Model Intercomparison Project (SIMIP):
834 understanding sea ice through climate-model simulations, *Geosci. Model Dev.*, 9, 3427–
835 3446, <https://doi.org/10.5194/gmd-9-3427-2016>, 2016.

836 Ogi, M., Yamazaki, K., and Wallace, J. M.: Influence of winter and summer surface wind
837 anomalies on summer Arctic sea ice extent, *Geophys. Res. Lett.*, 37, L07701,
838 doi:10.1029/2009GL042356, 2010.

839 Olonscheck, D., Mauritsen, T. and Notz, D.: Arctic sea-ice variability is primarily driven by
840 atmospheric temperature fluctuations. *Nat. Geosci.* 12, 430–434,
841 <https://doi.org/10.1038/s41561-019-0363-1>, 2019.

842 Padman, L., and Dillon, T. M.: Vertical heat fluxes through the Beaufort Sea thermohaline
843 staircase. *J. Geophys. Res.*, 92, 10 799–10 806,
844 <https://doi.org/10.1029/JC092iC10p10799>, 1987.

845 Perovich, D., Richter-Menge, J., Jones, K., Light, B., Elder, B., Polashenski, C., Laroche, D.,
846 Markus, T., and Lindsay, R.: Arctic sea-ice melt in 2008 and the role of solar heating.
847 *Annals of Glaciology*, 52(57), 355-359. doi:10.3189/172756411795931714, 2011.

848 Perovich, D., Richter-Menge, J., Polashenski, C., Elder, B., Arbetter, T., and Brennick, O.: Sea
849 ice mass balance observations from the North Pole Environmental Observatory,
850 *Geophys. Res. Lett.*, 41, 2019– 2025, doi:10.1002/2014GL059356, 2014.

851 Peterson, K., Arribas, A., Hewitt, H., Keen, A., Lea, D., and McLaren, A.: Assessing the
852 forecast skill of Arctic sea ice extent in the GloSea4 seasonal prediction system. *Climate*
853 *Dynamics*, 44(1-2), 147–162, 2015.

854 Pham, D. T.: Stochastic methods for sequential data assimilation in strongly nonlinear systems.
855 *Mon. Wea. Rev.*, 129, 1194–1207, 2001.

856 Rasch, P. J.: Conservative shape-preserving two-dimensional transport on a spherical reduced
857 grid, *Mon. Wea. Rev.*, 122, 1337-1350, 1994.

858 Reynolds, R. W., Smith, T. M., Liu, C., Chelton, D. B., Casey, K. S., and Schlax, M. G.: Daily
859 High-Resolution-Blended Analyses for Sea Surface Temperature, *Journal of Climate*,
860 20(22), 5473-5496, 2007.

861 Ricker, R., Hendricks, S., Kaleschke, L., Tian-Kunze, X., King, J., and Haas, C.: A weekly
862 Arctic sea-ice thickness data record from merged CryoSat-2 and SMOS satellite data,
863 The Cryosphere, 11, 1607–1623, <https://doi.org/10.5194/tc-11-1607-2017>, 2017.

864 Roach, L. A., Bitz, C. M., Horvat, C., and Dean, S. M.: Advances in modeling interactions
865 between sea ice and ocean surface waves. Journal of Advances in Modeling Earth
866 Systems, 11. <https://doi.org/10.1029/2019MS001836>, 2019.

867 Roach, L. A., Horvat, C., Dean, S. M., and Bitz, C. M.: An emergent sea ice floe size
868 distribution in a global coupled ocean–sea ice model. Journal of Geophysical Research:
869 Oceans, 123(6), 4322–4337. <https://doi.org/10.1029/2017JC013692>, 2018.

870 Rocheta, E., Evans, J. P., and Sharma, A.: Can Bias Correction of Regional Climate Model
871 Lateral Boundary Conditions Improve Low-Frequency Rainfall Variability?, Journal of
872 Climate, 30(24), 9785–9806, 2017.

873 Rocheta, E., Evans, J. P. and Sharma, A.: Correcting lateral boundary biases in regional climate
874 modelling: the effect of the relaxation zone. Clim. Dyn., 55, 2511–2521.
875 <https://doi.org/10.1007/s00382-020-05393-1>, 2020.

876 Serreze, M. C. and Meier, W. N.: The Arctic's sea ice cover: trends, variability, predictability,
877 and comparisons to the Antarctic. Ann. N.Y. Acad. Sci., 1436: 36–53.
878 <https://doi.org/10.1111/nyas.13856>, 2019.

879 Saha, S., Moorthi, S., Wu, X., et al.: The NCEP climate forecast system version 2. J. Clim.
880 27:2185–2208, 2014.

881 Schmidt, G. A., Bitz, C. M., Mikolajewicz, U., and Tremblay, L.-B.: Ice–ocean boundary
882 conditions for coupled models, Ocean Model., 7, 59–74, 2004.

883 Shchepetkin, A.F., McWilliams, J. C.: Quasi-monotone advection schemes based on explicit
884 locally adaptive dissipation. Mon. Weather Rev. 126 (6), 1541–1580, 1998.

885 Shchepetkin, A. F., and McWilliams, J. C.: The Regional Ocean Modeling System: A split-
886 explicit, free-surface, topography following coordinates ocean model, Ocean Modelling,
887 9, 347–404, 2005.

888 Shi, X., Notz, D., Liu, J., Yang, H., and Lohmann, G.: Sensitivity of Northern Hemisphere
889 climate to ice–ocean interface heat flux parameterizations, *Geosci. Model Dev.*, 14,
890 4891–4908, <https://doi.org/10.5194/gmd-14-4891-2021>, 2021.

891 Sigmond, M., Fyfe, J., Flato, G., Kharin, V., and Merryfield, W.: Seasonal forecast skill of
892 Arctic sea ice area in a dynamical forecast system. *Geophysical Research Letters*, 40,
893 529–534. <https://doi.org/10.1002/grl.50129>, 2013.

894 Skamarock, W. C., Klemp, J. B., Dudhia, J., Gill, D. O., Barker, D. M., Wang, W. and Powers,
895 J. G.: A Description of the Advanced Research WRF Version 2. NCAR Technical Note,
896 NCAR/TN-468+STR, 2005.

897 Smolarkiewicz, P. K.: Multidimensional positive definite advection transport algorithm: An
898 overview. *Int. J. Numer. Methods Fluids*, 50, 1123–1144, 2006.

899 Song, Y. and Haidvogel, D. B.: A semi-implicit ocean circulation model using a generalized
900 topography-following coordinate system. *J. Comp. Phys.*, 115(1), 228-244, 1994.

901 Steele, M.: Sea ice melting and floe geometry in a simple ice-ocean model. *Journal of*
902 *Geophysical Research: Oceans*, 97(C11), 17,729–17,738.
903 <https://doi.org/10.1029/92JC01755>, 1992.

904 Stroeve, J., Blanchard-Wrigglesworth, E., Guemas, V., Howell, S., Massonnet, F., and Tietsche,
905 S.: Improving predictions of Arctic sea ice extent, *Eos*, 96,
906 <https://doi.org/10.1029/2015EO031431>, 2015.

907 Stroeve, J., Hamilton, L. C., Bitz, C. M., and Blanchard-Wrigglesworth, E.: Predicting
908 September sea ice: Ensemble skill of the SEARCH Sea Ice Outlook 2008 – 2013,
909 *Geophys. Res. Lett.*, 41, 2411-2418, <https://doi.org/10.1002/2014GL059388>, 2014.

910 Tian-Kunze, X., Kaleschke, L., Maaß, N., Mäkynen, M., Serra, N., Drusch, M., and Krumpen,
911 T.: SMOS-derived thin sea ice thickness: Algorithm baseline, product specifications and
912 initial verification. *Cryosphere*, 8, 997-1018, <https://doi.org/10.5194/tc-8-997-2014>,
913 2014.

914 Tietsche, S., Day, J., Guemas, V., Hurlin, W., Keeley, S., Matei, D., et al.: Seasonal to
915 interannual Arctic sea ice predictability in current global climate models. *Geophysical*
916 *Research Letters*, 41, 1035–1043. <https://doi.org/10.1002/2013GL058755>, 2014.

917 Tsamados, M., Feltham, D. L., and Wilchinsky, A. V.: Impact of a new anisotropic rheology
918 on simulations of Arctic sea ice, *J. Geophys. Res. Oceans*, 118, 91–107,
919 doi:10.1029/2012JC007990, 2013.

920 Turner, A. K., and Hunke, E. C.: Impacts of a mushy-layer thermodynamic approach in global
921 sea-ice simulations using the CICE sea-ice model, *J. Geophys. Res. Oceans*, 120, 1253-
922 1275, doi:10.1002/2014JC010358, 2015.

923 Turner, A. K., Hunke, E. C., and Bitz, C. M.: Two modes of sea-ice gravity drainage: A
924 parameterization for large-scale modeling, *J. Geophys. Res.*, 118, 2279–2294,
925 doi:10.1002/jgrc.20171, 2013.

926 Turner, J. S.: *Buoyancy Effects in Fluids*. Cambridge University Press, 368 pp. 1973.

927 Van den Dool, H.: *Empirical Methods in Short-Term Climate Prediction*, Oxford Univ. Press,
928 Oxford, U. K., 2006.

929 Wang, W., Chen, M., and Kumar, A.: Seasonal prediction of Arctic sea ice extent from a
930 coupled dynamical forecast system. *Monthly Weather Review*, 141(4), 1375–1394, 2013.

931 Warner, J. C., Armstrong, B., He, R., and Zambon, J.: Development of a coupled ocean–
932 atmosphere–wave–sediment transport (COAWST) modeling system. *Ocean Modell.* 35,
933 230–244, 2010.

934 Woodgate, R. A., Aagaard, K., and Weingartner, T. J.: A year in the physical oceanography of
935 the Chukchi Sea: Moored measurements from autumn 1990–1991. *Deep-Sea Res. II*, 52,
936 3116–3149, <https://doi.org/10.1016/j.dsr2.2005.10.016>, 2005.

937 Wu, W., Lynch, A. H., and Rivers, A.: Estimating the Uncertainty in a Regional Climate Model
938 Related to Initial and Lateral Boundary Conditions, *Journal of Climate*, 18(7), 917-933,
939 2005.

940 Yang, C.-Y., Liu, J., and Xu, S.: Seasonal Arctic sea ice prediction using a newly developed
941 fully coupled regional model with the assimilation of satellite sea ice observations.
942 Journal of Advances in Modeling Earth Systems, 12, e2019MS001938.
943 <https://doi.org/10.1029/2019MS001938>, 2020.

944 Zampieri, L., Goessling, H. F., and Jung, T.: Bright prospects for Arctic sea ice prediction on
945 subseasonal time scales. Geophysical Research Letters, 45, 9731– 9738.
946 <https://doi.org/10.1029/2018GL079394>, 2018.

947 Zhang, J. and Rothrock, D.: Modeling global sea ice with a thickness and enthalpy distribution
948 model in generalized curvilinear coordinates. Mon. Wea. Rev., 131, 845–861, 2003.

949 Zhang, J., Lindsay, R., Steele, M., and Schweiger, A.: What drove the dramatic retreat of arctic
950 sea ice during summer 2007?, Geophys. Res. Lett., 35, L11505,
951 [doi:10.1029/2008GL034005](https://doi.org/10.1029/2008GL034005), 2008.

952 Zhang, J., Schweiger, A., Steele, M., and Stern, H.: Sea ice floe size distribution in the marginal
953 ice zone: Theory and numerical experiments. Journal of Geophysical Research: Oceans,
954 120, 3484–3498. <https://doi.org/10.1002/2015JC010770>, 2015.

955 Zhang, J., Stern, H., Hwang, B., Schweiger, A., Steele, M., Stark, M., and Graber, H. C.:
956 Modeling the seasonal evolution of the Arctic sea ice floe size distribution. Elementa:
957 Science of the Anthropocene, 4(1), 126.
958 <https://doi.org/10.12952/journal.elementa.000126>, 2016.

959

960 **7. Tables**

961 Table 1 The summary of physic parameterizations used in the Y21_CRTL experiment

WRF physics	
Cumulus parameterization	Grell-Freitas (Freitas et al. 2018; improved from Y20)
Microphysics parameterization	Morrison 2-moment (Morrison et al. 2009; same as Y20)
Longwave radiation parameterization	CAM spectral band scheme (Collins et al. 2004; same as Y20)
Shortwave radiation parameterization	CAM spectral band scheme (Collins et al. 2004; same as Y20)
Boundary layer physics	MYNN2 (Nakanishi and Niino, 2006; improved from Y20)
Land surface physics	Unified Noah LSM (Chen and Dudhia, 2001; improved from Y20)
ROMS physics	
Tracer advection scheme	MPDATA (Smolarkiewicz, 2006; same as Y20)
Tracer vertical mixing scheme	GLS (Umlauf and Burchard, 2003; same as Y20)

Bottom drag scheme	Quadratic bottom friction (QDRAG; (same as Y20)
CICE physics	
Ice dynamics	EVP (Hunke and Dukowicz, 1997; improved from Y20)
Ice thermodynamics	Bitz and Lipscomb (1999; same as Y20)
Shortwave albedo	Delta-Eddington (Briegleb and Light, 2007; same as Y20)

962

963

964 Table 2 The summary of the prediction experiments and details of experiment designs.

965 Note: All experiments use the CFS operational forecasts as initial and boundary conditions; VT:

966 vertical transformation function; VS: vertical stretching function; SH94: stretching function of

967 Song and Haidvogel (1994); S10: stretching function of Shchepetkin (2010).

Experiment	Physics	Assimilation	ROMS vertical coordinate	Simulation period
Y20_MOD	Physics (old version) listed in Table 1	6 localization radii SSMIS SIC Simply-merged CryoSat- 2/SMOS SIT	VT 1 VS SH94 h_c 10m	2018.07.01- 2018.10.01
Y21_CTRL	Physics (new version) listed in Table 1	6 localization radii SSMIS SIC Simply-merged CryoSat- 2/SMOS SIT	VT 1 VS SH94 h_c 10m	2018.07.01- 2018.10.01
Y21_VT	Physics (new version) listed in Table 1	6 localization radii SSMIS SIC Simply-merged CryoSat- 2/SMOS SIT	VT 2 VS S10 h_c 300m	2018.07.01- 2018.10.01
Y21_RP	Advection: U3H/C4V	6 localization radii	VT 2	2018.07.01-

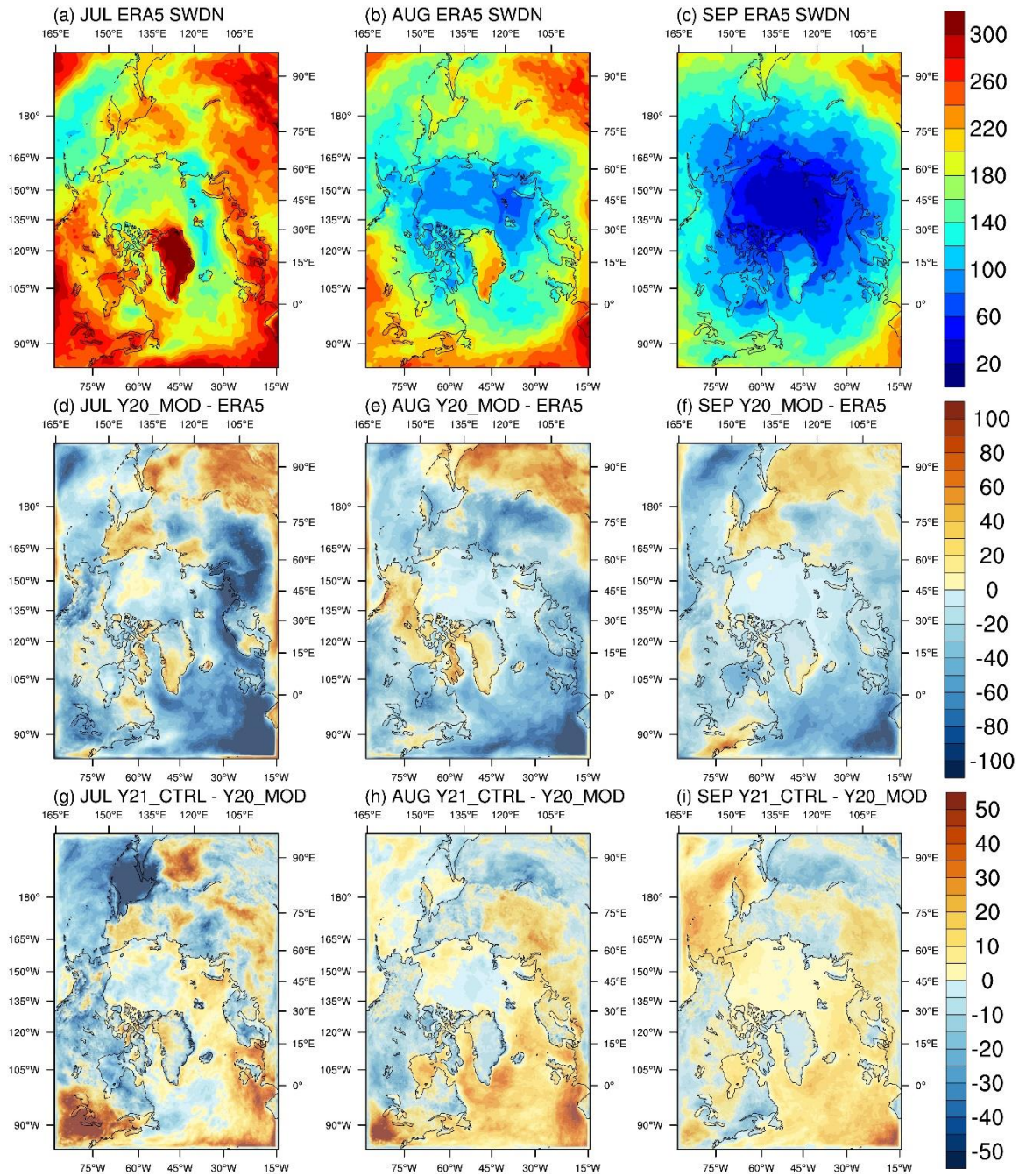
		SSMIS SIC Simply-merged CryoSat- 2/SMOS SIT	VS S10 h_c 300m	2018.10.01
Y21_MUSHY	Same physics as Y21_RP CICE: Mushy layer thermodynamics	6 localization radii SSMIS SIC Simply-merged CryoSat- 2/SMOS SIT	VT 2 VS S10 h_c 300m	2018.07.01- 2018.10.01
Y21_SIT	Same physics as Y21_RP	6 localization radii SSMIS SIC OI-merged CryoSat- 2/SMOS SIT	VT 2 VS S10 h_c 300m	2018.07.01- 2018.10.01
Y21_EXT-7	Same physics as Y21_RP	6 localization radii SSMIS SIC OI-merged CryoSat- 2/SMOS SIT	VT 2 VS S10 h_c 300m	2018.07.01- 2019.01.31

|
970

971

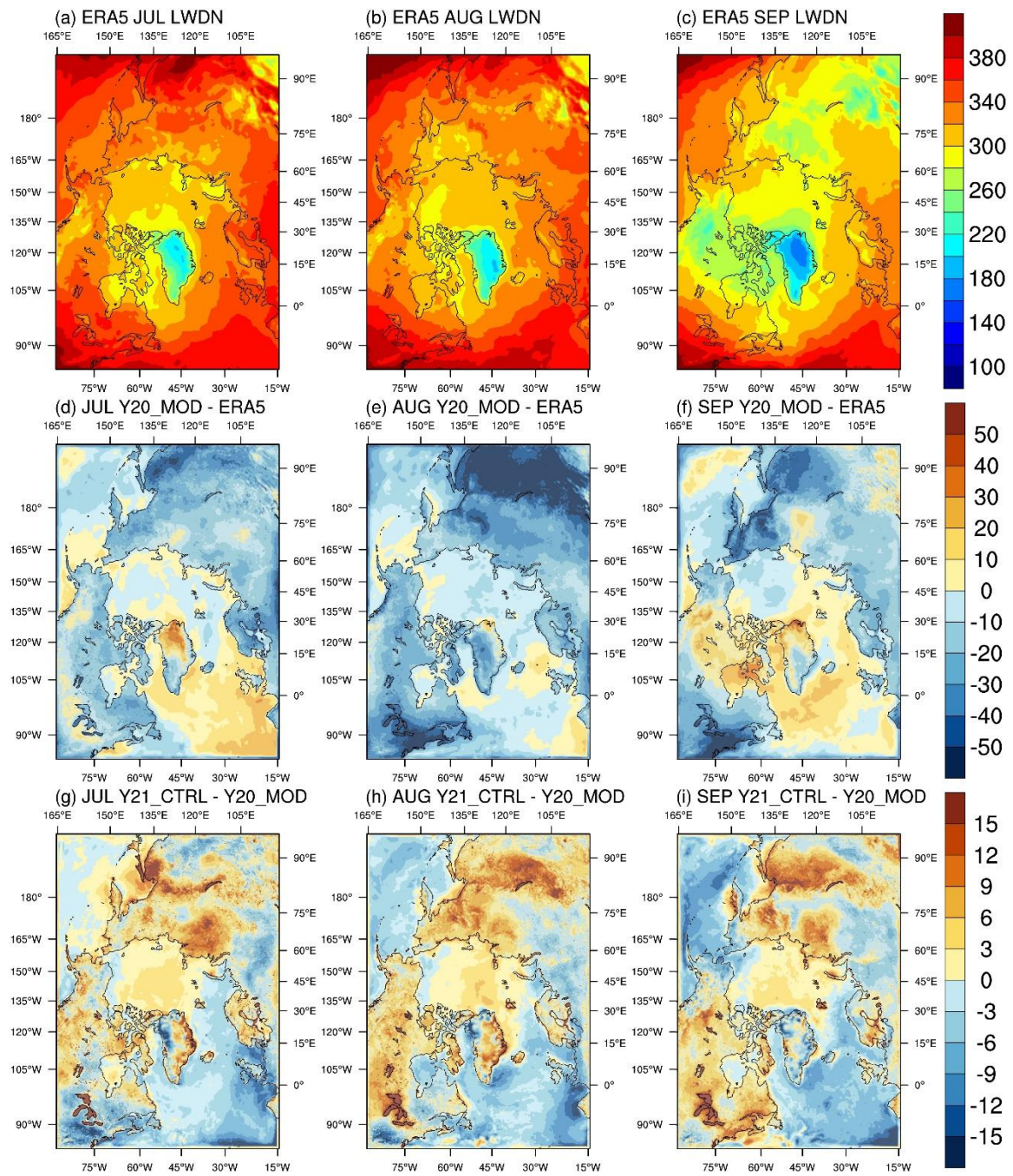
删除了: Y

973 **8. Figures**



974
 975 Figure 1 ERA5 monthly mean of downward shortwave radiation at the surface for (a) July, (b)
 976 August, and (c) September, the difference between Y20_MOD and ERA5 for (d) July, (e)
 977 August, (f) September, and the difference between Y21_CTRL (changes in the atmospheric
 978 physics) and Y20_MOD (the original CAPS) for (g) July, (h) August, and (i) September.

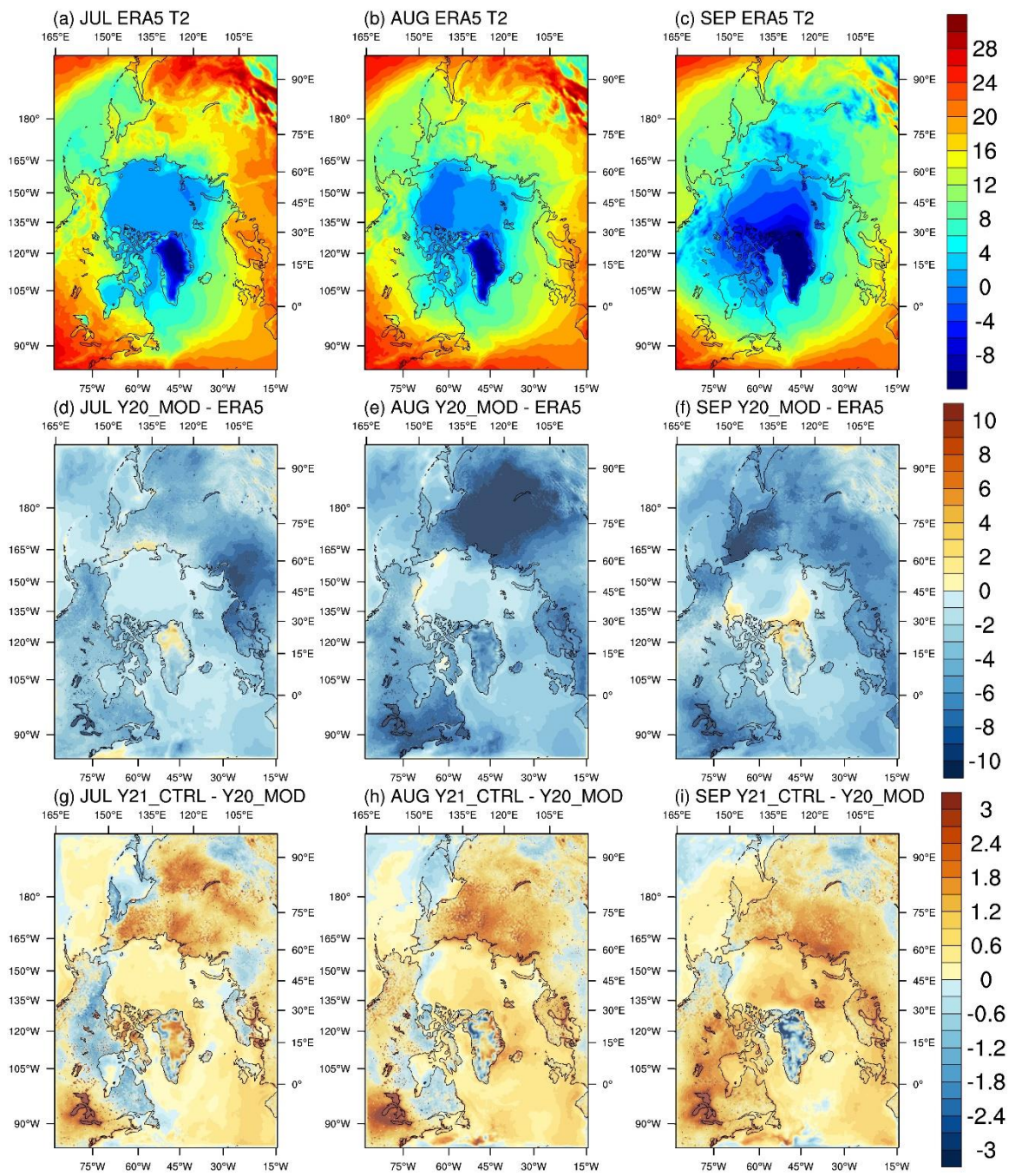
979



980

981 Figure 2 Same as Figure 1, but for downward thermal radiation at the surface.

982

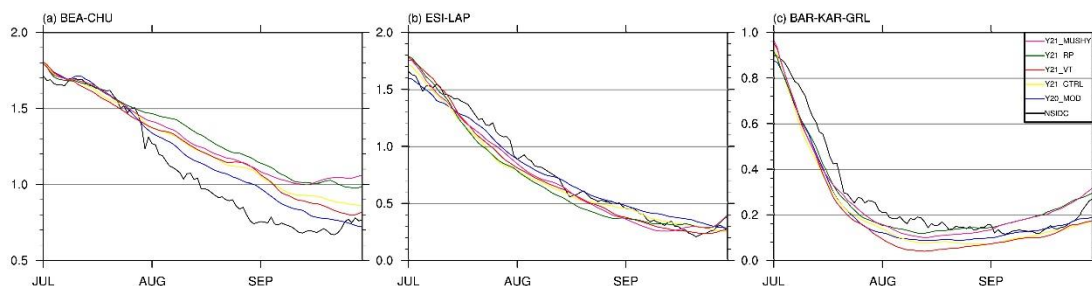
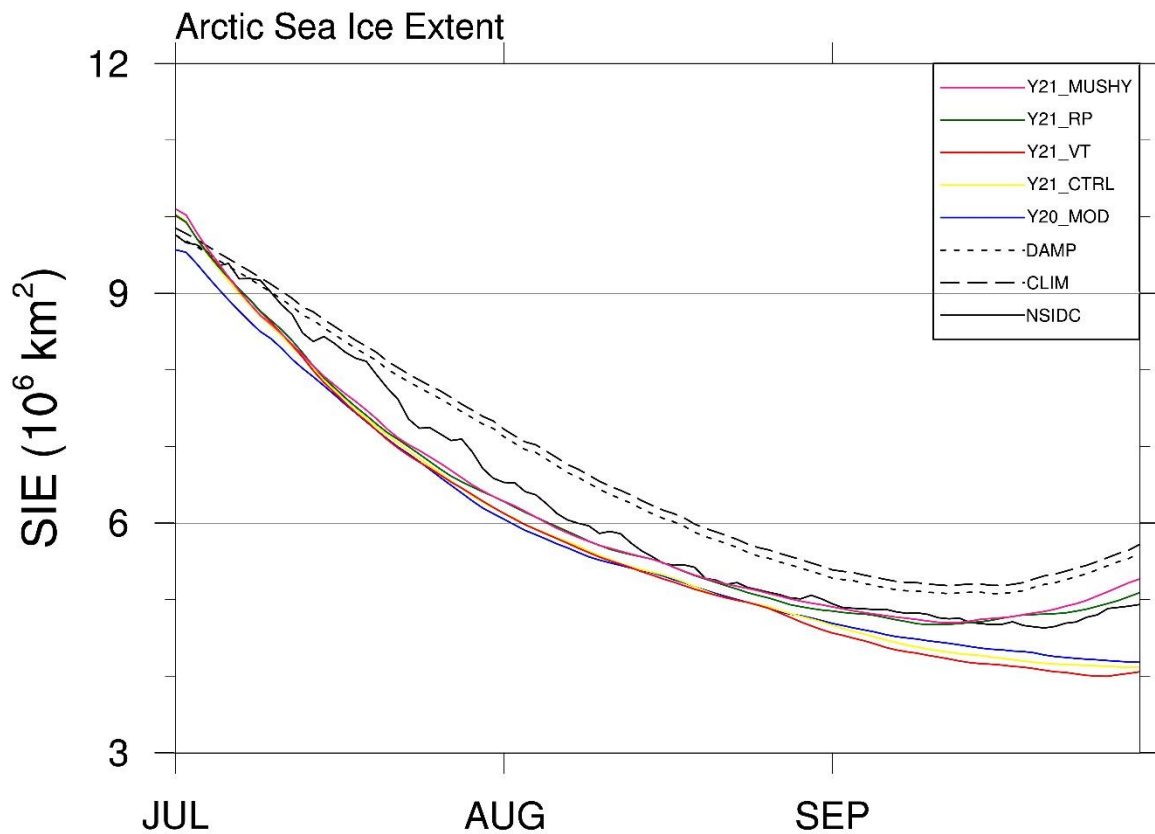


983

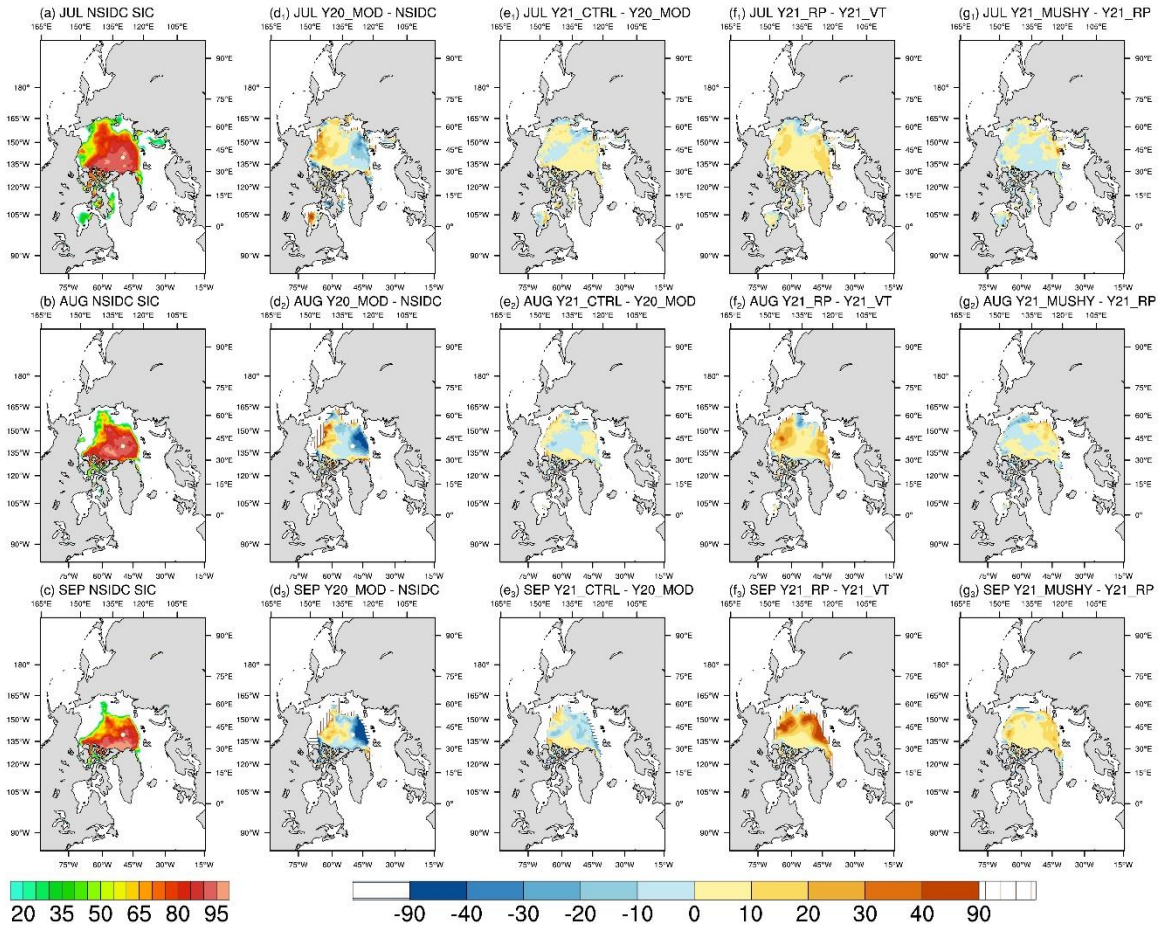
984 Figure 3 Same as Figure 1, but for near-surface air temperature.

985

986



987
 988 Figure 4 Top panel: Time-series of Arctic sea ice extent for the observations (black line) and
 989 the ensemble-mean of Y20_MOD (blue line, the original CAPS), Y21_CTRL (yellow line,
 990 changes in the atmospheric physics), Y21_VT (red line, changes in the ocean vertical
 991 coordinate), Y21_RP (green line, changes in the oceanic advection), and Y21_MUSHY (pink
 992 line, changes in sea ice thermodynamics). Dashed and dotted lines are the climatology and the
 993 damped anomaly persistence predictions. Bottom panel: Time-series of the observed (black
 994 line) and the ensemble-mean of regional sea ice extents for Y20_MOD (blue line), Y21_CTRL
 995 (yellow line), Y21_VT (red line), Y21_RP (green line), and Y21_MUSHY (pink line) for (a)
 996 Beaufort-Chukchi Seas, (b) East Siberian-Laptev Seas, and (c) Barents-Kara-Greenland Seas.



997

998

999

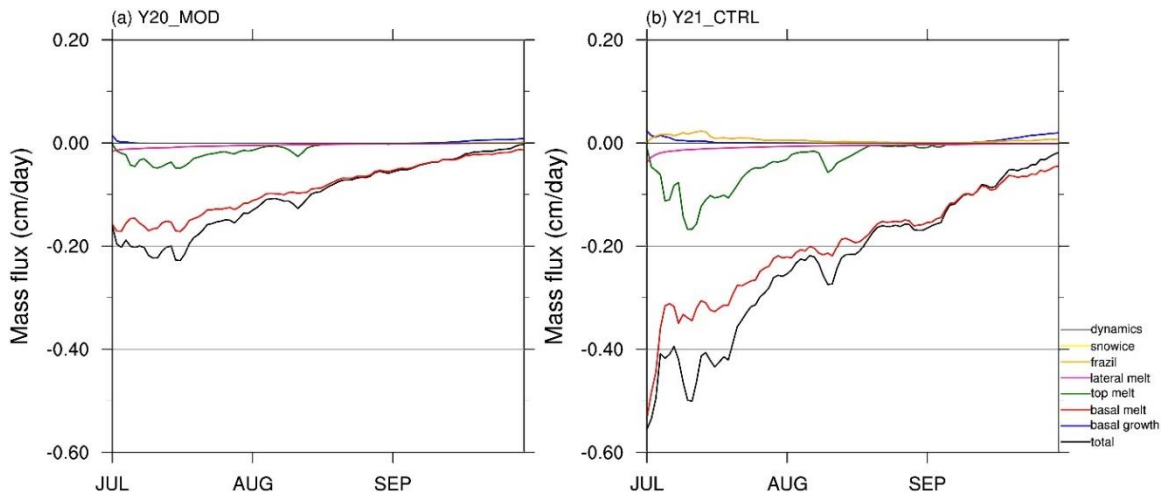
1000

1001

1002

Figure 5 Monthly mean of sea ice concentration for (a) July, (b) August, (c) September of the NSIDC observations, and the difference between the all prediction experiments and the observations for (d₁-g₁) July, (d₂-g₂) August, (d₃-g₃) September. Vertical/horizontal-line areas represent the difference of ice edge location (15% concentration).

1003



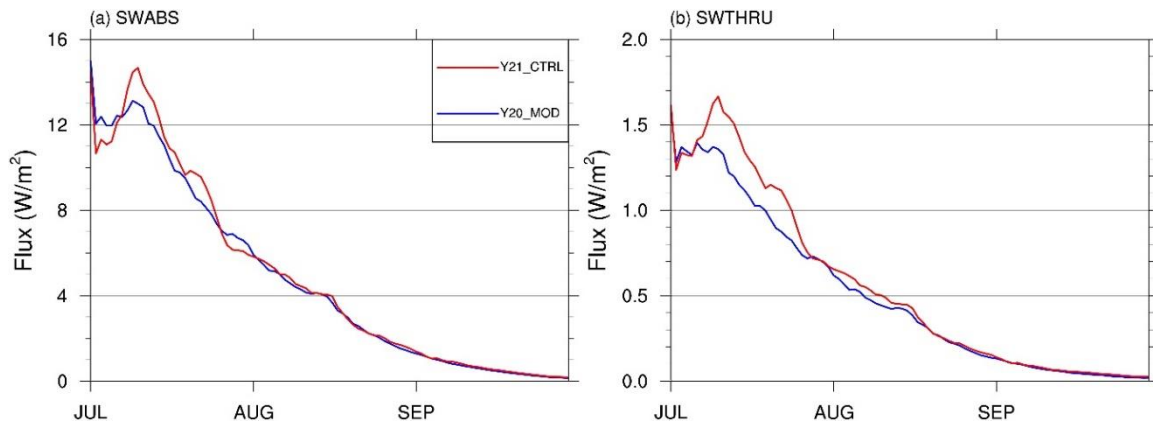
1004

1005 Figure 6 Time-series of sea ice mass budget terms for (a) Y20_MOD (the original CAPS) and

1006 (b) Y21_CTRL (changes in the atmospheric physics).

1007

1008



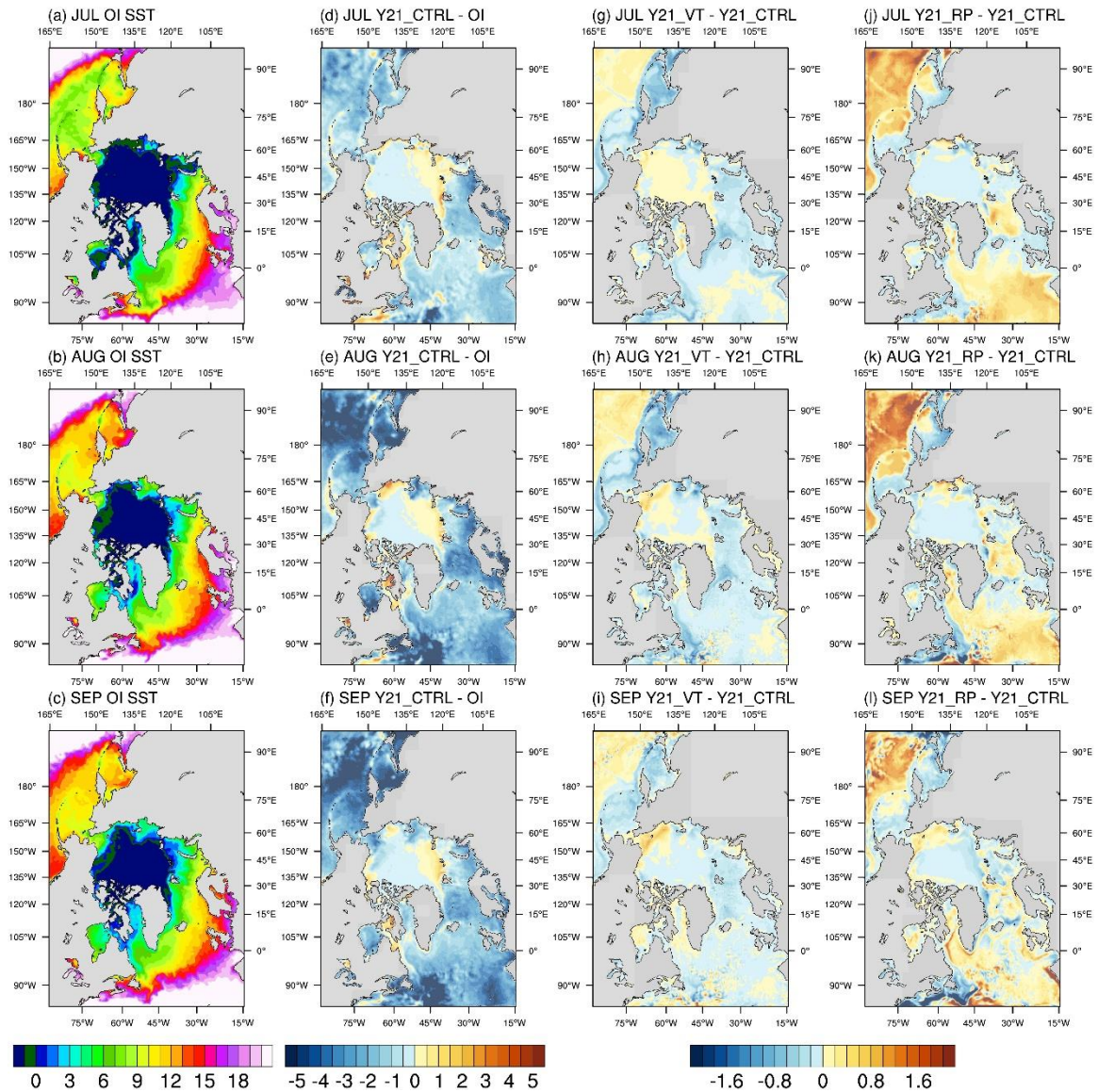
1009

1010 Figure 7 Time-series of (a) shortwave radiation absorbed by ice surface, and (b) penetrating

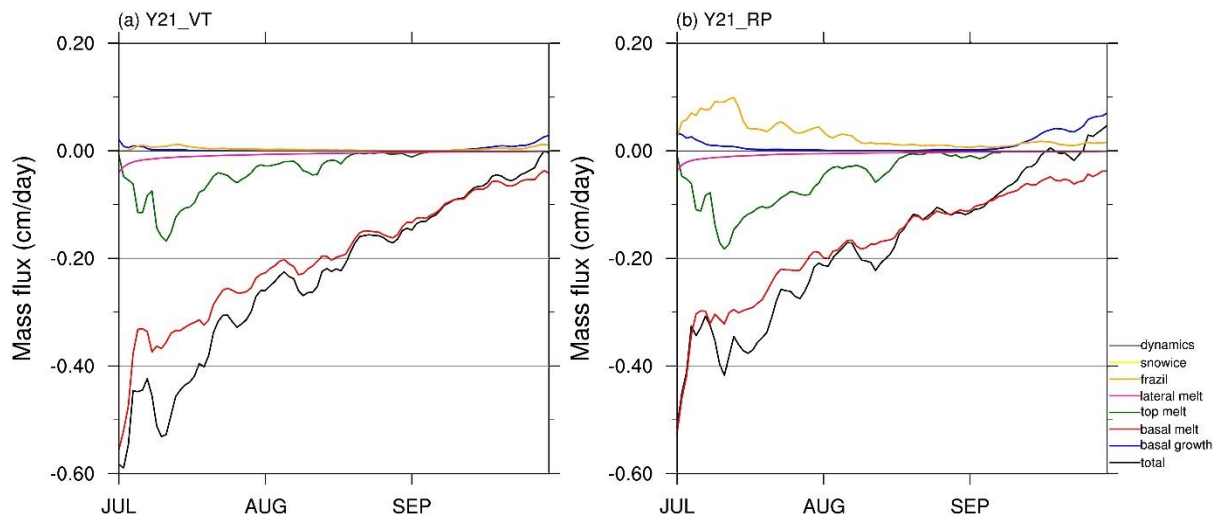
1011 shortwave radiation to the upper ocean averaged over ice-covered grid cells for Y20_MOD

1012 (blue line, the original CAPS) and Y21_CTRL (red line, changes in the atmospheric physics).

1013



1014
 1015 Figure 8 First column: monthly mean of sea surface temperature for (a) July, (b) August, (c)
 1016 September of the OI SST. Second column: the difference between Y21_CTRL and the OI SST
 1017 for (d) July, (e) August, (f) September. Right panel: Monthly mean of sea surface temperature
 1018 difference between Y21_VT/Y21_RP and Y21_CTRL for (g) July, (h) August, (i) September
 1019 of Y21_VT, (j) July, (k) August, and (l) September of Y21_RP.
 1020

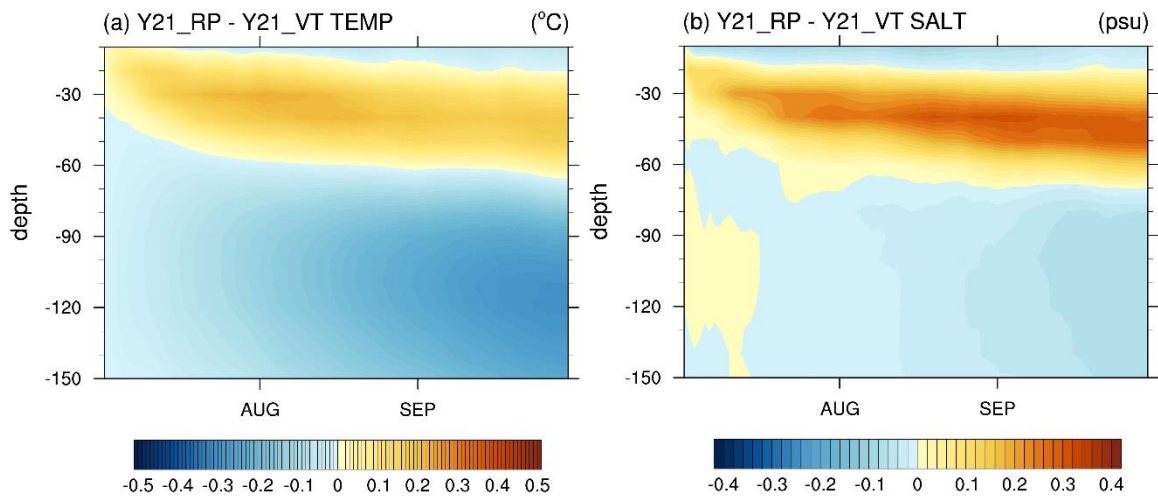


1021

1022 Figure 9 Same as Figure 6, but for (a) Y21_VT (changes in the ocean vertical coordinate), and

1023 (b) Y21_RP (changes in the oceanic advection).

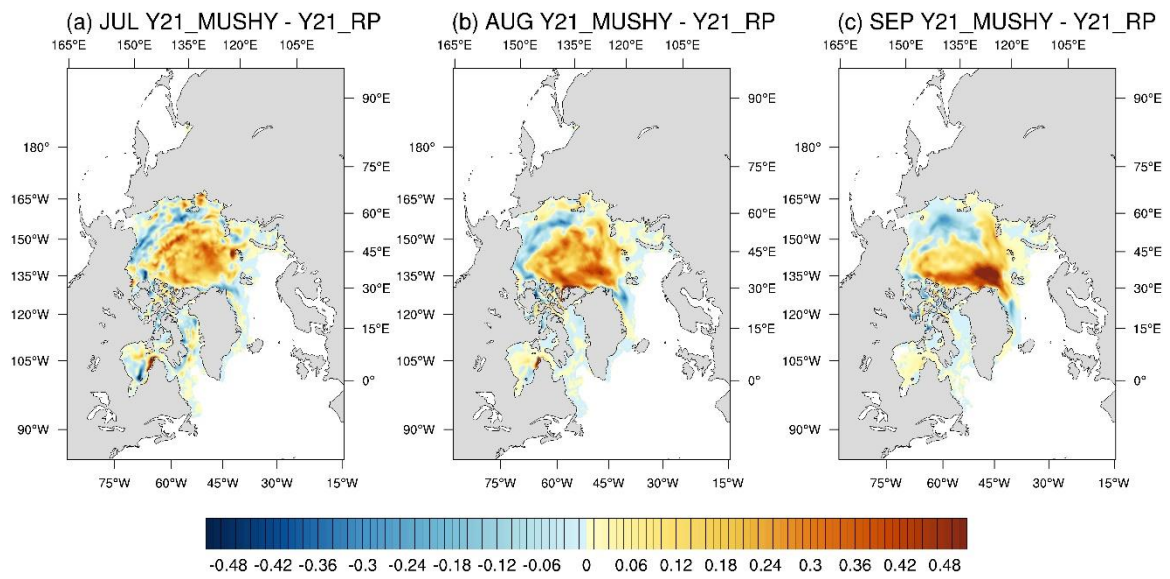
1024



1025

1026 Figure 10 (a) the average temperature profile of upper 150 m under ice-covered areas for the
1027 difference between Y21_RP and Y21_VT. (b) same as (a), but for the salinity profile.

1028

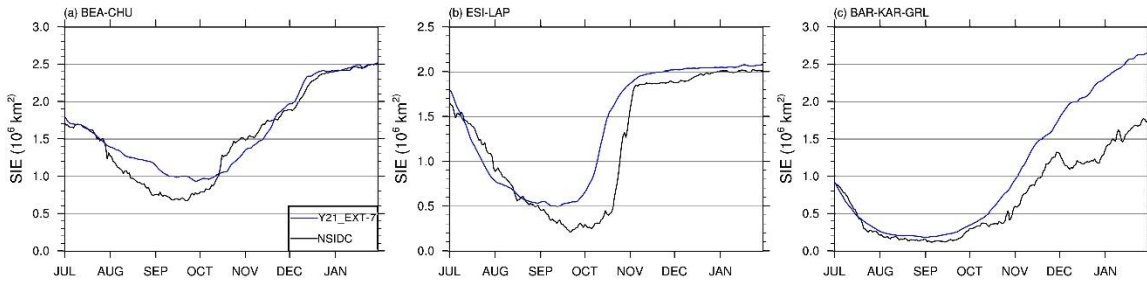
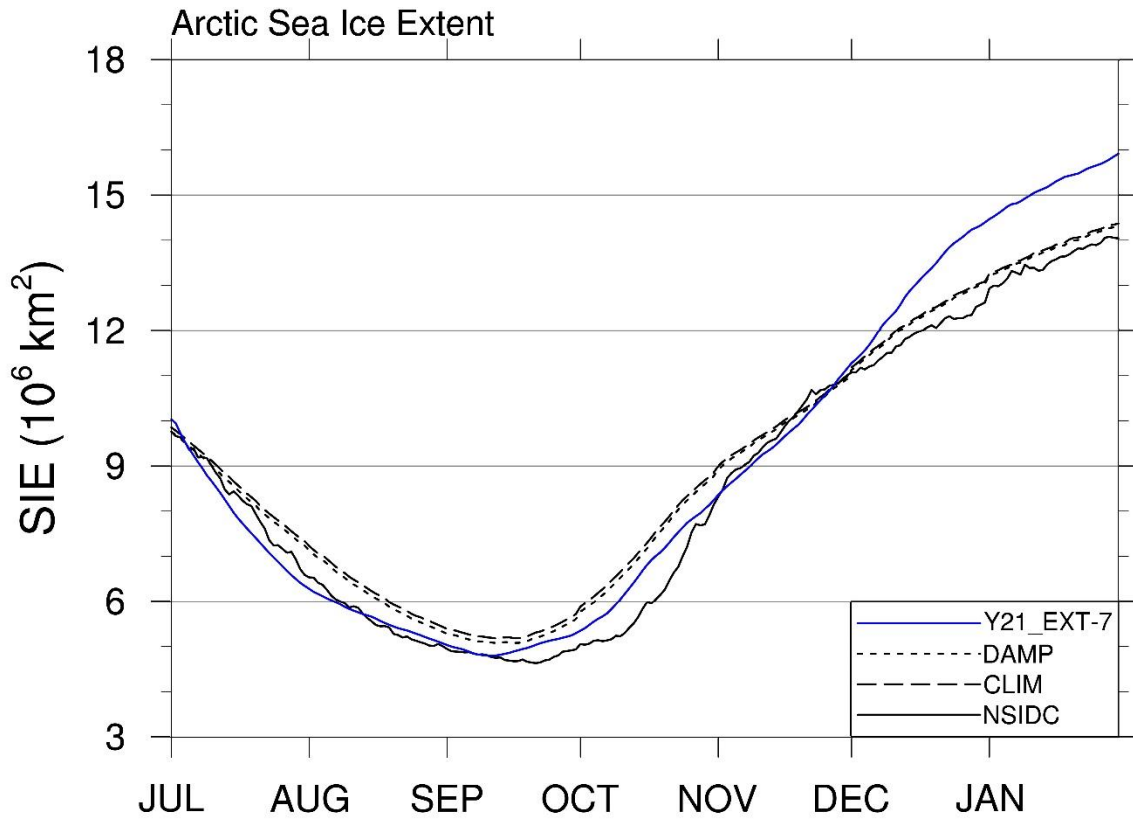


1029

1030

1031

Figure 11 Monthly mean of sea ice thickness difference between Y21_MUSHY (changes in sea ice thermodynamics) and Y21_RP for (a) July, (b) August, and (c) September.



1032

1033 Figure 12 Same as Figure 4, but for Y21_EXT-7.

1034

